Chapter 2
Solid-State Detectors for Small-Animal Imaging

Paolo Russo and Alberto Del Guerra

1 Introduction

Semiconductor detector technology, initially developed for high energy physics applications, has found a distinctive role in high performance systems for X-ray and gamma-ray medical imaging applications, including small animal imaging. Single-Photon Emission Computed Tomography (SPECT) small animal imaging requires the development of compact detectors with intrinsically ultrahigh spatial resolution, high energy resolution and good detection efficiency, in addition to suitable radiation collimation strategies. This overall performance can only partly be guaranteed by scintillator based systems with photomultiplier tube readout, the most used technology at present for small animal SPECT scanners. On the other hand, with respect to scintillator based detectors, semiconductor detectors can offer a gain by approximately a factor two in energy resolution at typical radionuclide energies, a factor greater than two in intrinsic spatial resolution, and a comparable intrinsic detection efficiency, though usually at a reduced field of view. Moreover, their compactness could be crucial in devising animal "personalized" miniature scanners. An additional interesting feature of semiconductor based small animal SPECT scanners is that the detector technology can be used both for gamma-ray imaging and for X-ray imaging, when coupling the SPECT scanner to a low resolution X-ray CT scanner for anatomical registration. The requirement of high spatial resolution, coupled to high sensitivity, becomes also stringent in microPET systems, where semiconductor detectors could be the technology of choice for future high performance PET scanners.

P. Russo (✉)
Dipartimento di Fisica, Università di Napoli Federico II,
and INFN Sezione di Napoli, Napoli, Italy
e-mail: Paolo.Russo@na.infn.it

A. Del Guerra
Dipartimento di Fisica, Università di Pisa, and INFN Sezione di Pisa, Pisa, Italy
e-mail: alberto.delguerra@df.unipi.it
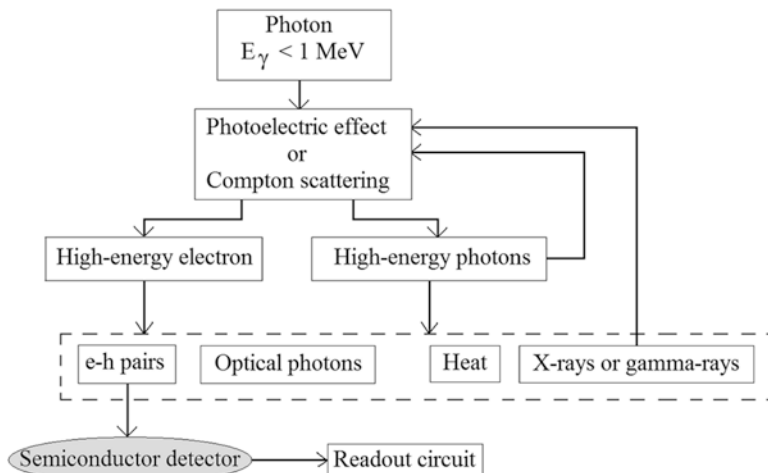
Fig. 2.1 Schematics of the inelastic interaction of a gamma ray in the detector material, up to energies below 1 MeV

This chapter illustrates the basic technology of pixel and microstrip semiconductor detectors for these small animal imaging applications, with reference to the most used technologies, relative to the CdTe, CdZnTe (CZT) and Si semiconductors. Still at its early stage, but of increasing interest, is the technology of semiconductor detectors—CdTe, CdZnTe, Si room-temperature semiconductors, in addition to liquid nitrogen cooled Ge—specifically for Positron Emission Tomography (PET) in ultra high resolution small animal scanners. Examples of development of semiconductor SPECT and SPECT/CT scanners, and of semiconductor PET scanners for small animal imaging, are presented. In illustrating those systems, the emphasis will be on their technical description.

In order to illustrate the application of semiconductor detectors to small animal imaging in the area of microSPECT and microPET, a brief outline follows on the physical characteristics of those detectors. Basic terminology, relevant data and basic techniques will be introduced for completeness of illustration.

1.1 Basic Principles of Radiation Semiconductor Detectors

Semiconductor detectors for X-rays and gamma-rays in the diagnostic energy range for radiography and nuclear medicine (from tens of keV up to some hundreds of keV) work by converting the energy of interacting photons into a number of electron–hole (e–h) pairs transported to the corresponding collection electrodes and then by recording this charge (Fig. 2.1). Once a photoelectric or a Compton interaction occurs in the semiconductor substrate, a high-kinetic-energy electron is created. The probability of this event determines the quantum efficiency of the detector.

Table 2.1 Physical properties of some semiconductors for X-ray and gamma-ray imaging [2]

	Material			
	Si	CdTe	$Cd_{0.9}Zn_{0.1}Te$	Ge
Atomic number(s)	14	48; 52	48; 30; 52	32
Effective atomic number	14	50	49.1	32
Density (g/cm³)	2.33	5.85	5.78	5.33
Bandgap, E_g (eV)	1.12	1.44	1.572	0.67
Electron mobility, μ_e (cm²/V s)	1,400	1,100	1,000	3,900
Electron lifetime, τ_e (s)	$>10^{-3}$	3×10^{-6}	3×10^{-6}	$>10^{-3}$
Hole mobility, μ_h (cm²/V s)	480	100	50–80	1,900
Hole lifetime, τ_h (s)	2×10^{-3}	2×10^{-6}	10^{-6}	10^{-3}
$\mu_e\tau_e$ (cm²/V)	>1	3.3×10^{-3}	$3–5 \times 10^{-3}$	>1
$\mu_h\tau_h$ (cm²/V)	1	2×10^{-4}	5×10^{-5}	>1
Pair creation energy (eV/e–h pairs)	3.62	4.43	4.64	2.95
Dielectric constant	11.7	11	10.9	16
Resistivity (Ω cm) @ 20 °C	$<10^4$	10^9	3×10^{10}	50

This high energy electron loses its energy in the material by producing phonons and energetic e–h pairs, and these electrons and holes can, in turn, produce phonons or create secondary e–h pairs, up to the end of their energy loss process where they recombine radiatively or through phonon excitation [1].

Semiconductor detectors collect the electrons and holes and produce a signal in the readout circuit. Since a part of the charge created can be trapped in semiconductor bulk or anyway is unable to contribute to the electrical signal at the collecting electrode, the charge collection efficiency (CCE) can be less than unity: this occurs, e.g., with compound semiconductor detectors in the presence of impurities, crystal defects, trapping centers etc. The amount of energy deposited in the detector volume by each interacting photon is directly proportional to the total number of e–h pairs created: for semiconductors, this pair creation energy is roughly in the range 3–5 eV/e–h pair (Table 2.1), against, e.g., 13 eV/e–h pair in NaI:Tl scintillator material. This implies a large signal generated in the semiconductor detector: for example, in CdTe a 100-keV photon can generate an average number of ≅23,000 e–h pairs, so that even in the presence of inefficiencies in the transport and collection of electron and hole charges, the electric signal can be conveniently amplified and the interaction event recorded. To this purpose, the detector dark (leakage) current must be kept low, so that the radio-induced signal is well separated from the detector noise.

There are two basic schemes for working in low-dark current conditions, which employ the diode structure (junction) or the resistive mode. In the first scheme (Fig. 2.2, which illustrates the case of high resistivity n-type Si wafers) p-n junctions are realized on the doped detector substrate by implanting p⁺ regions on one side in the form of single detector elements or multi-detector elements (strips, pixels) and n⁺ regions are on the opposite side. Then this diode structure is reverse-biased: in this case the leakage current flowing in the external circuit is largely reduced with respect to forward bias operation.
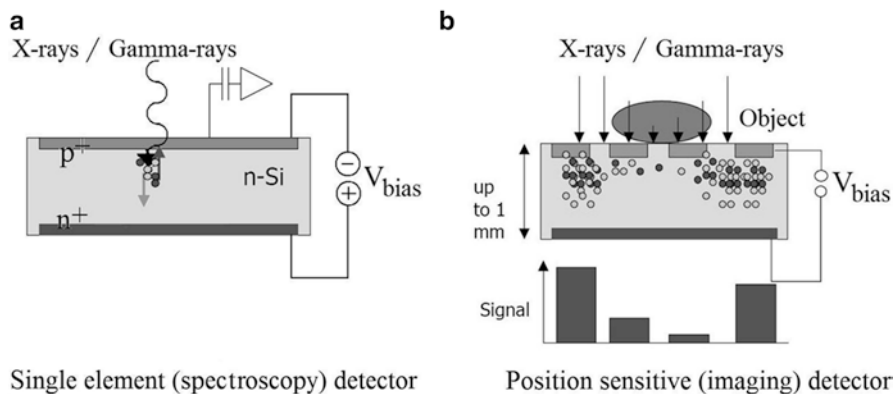
Fig. 2.2 Basic scheme of Si p–n junction detectors for spectroscopy (single element, **a**) or imaging applications (**b**), illustrating the generation, drift and collection of e–h pairs from interacting X-rays or gamma-rays

1.2 Charge Generation and Transport in Semiconductor Detectors

Application of a suitable high reverse bias voltage (increasing with the square of the substrate thickness) allows to extend the depletion (active) region to the whole detector thickness. Once fully depleted, the bias voltage can be further increased (before breakdown) in order to increase the strength E of the electric field in the drift region of the charge carriers. Alternatively, the (reverse biased) diode structure with a surface barrier can be realized by metal–semiconductor (Schottky) anode contact on one side, and low-resistive ("ohmic" or "injecting") metal–semiconductor contact on the opposite side (Fig. 2.3). This structure is used, e.g., with CdTe room-temperature compound semiconductors by using indium (or titanium/indium) for the anode electrode (which forms a high Schottky barrier at the In/CdTe interface) and platinum for the cathode electrode; alternatively, p-n junction type contacts can be created. In the second scheme (Fig. 2.3), photoconductive operation can be implemented by depositing ohmic contacts on both opposite sides of the detector substrate (e.g., in a Pt/CdTe/Pt detector). The irradiation geometry is typically head-on and from the cathode, but edge-on irradiation can be used as well (Fig. 2.3a), e.g. with thin detectors, in order to exploit a higher interaction depth and to assure good lateral resolution. Application of a high voltage bias assures high E values (e.g., 10^3–10^4 V/cm) and, hence, high drift velocities ($v_e = \mu_e \cdot E$; $v_h = \mu_h \cdot E$, with μ_e and μ_h electrical mobilities for electrons and holes, respectively) of the charge carriers generated by the interacting radiation. Then, in order to keep the leakage current low in photoconductive detectors, the semiconductor detector substrate must have a high bulk resistivity (e.g., 10^8–10^{10} Ω cm) (Table 2.1). Choice of the voltage polarity on
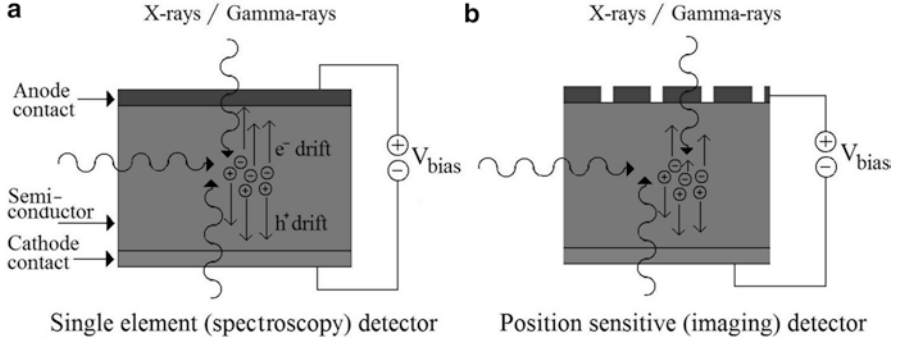
Fig. 2.3 Radiation detectors for spectroscopy (single element, **a**) or imaging applications with segmented contact electrodes (**b**) can be realized on semiconductor substrates equipped with ohmic or with Schottky contacts. As shown by the photon paths, they can be irradiated from the front side, from the back side or edge-on

the signal readout side allows to select the charge carrier type (electrons or holes), on dependence of their different electrical mobilities μ_e and μ_h, and on their lifetime τ_e, τ_h, respectively.

Due to presence of electronic levels in the forbidden gap region of the semiconductor corresponding to crystal defects, some electrons and holes are trapped in those levels during the drift process, reducing the values of τ_e, τ_h for compound semiconductors (e.g., CdTe, CdZnTe) to levels ($\cong \mu s$) orders of magnitude lower than for Si and Ge ($\cong$ ms) (Table 2.1). Typically, charge transport parameters (μ, τ), are significantly higher for electrons than for holes and these low μ_h, τ_h values cause hole trapping and charge loss. This asymmetry of charge carrier transport between electrons and holes introduces a dependence of the pulse shape and of the induced charge at the anode and cathode collecting electrodes, respectively, on the depth of interaction, z, inside the semiconductor detector active thickness, L. If the interaction event occurs close to the cathode ($z \cong 0$), hole movement contributes little to the charge signal. For interaction at a depth $0 \ll z < L$ from the cathode, the charge pulse shape depends on the contribution of holes. If the hole drift distance z from the cathode is long compared to the average distance before trapping $\lambda_h = v_h \cdot \tau_h = \mu_h \cdot \tau_h \cdot E$, then the CCE for the induced charge signal Q_{anode} at the anode is reduced, according to the following Hecht relation (where q is the elementary charge and N_0 is the number of e–h pairs created by the interacting photon at depth z):

$$CCE = \frac{Q_{anode}}{qN_0} = \frac{\mu_e \tau_e E}{L}\left(1 - e^{-(L-z)/\mu_e \tau_e E}\right) + \frac{\mu_h \tau_h E}{L}\left(1 - e^{-z/\mu_h \tau_h E}\right).$$

Due to the low $\mu_h \cdot \tau_h$ value, the above relationship shows that if the detector thickness L is greater than $\mu_h \cdot \tau_h \cdot E$, the collected charge Q_{anode} is less than qN_0 by a variable quantity in dependence of the interaction depth z. This implies that the peak spectral shape due to photoelectric absorption of a gamma ray presents a shoulder (tailing)

on the lower-energy side. For example, for CdTe, with the data in Table 2.1, and from the above equation, in a 1-mm thick detector biased at −100 V, the estimated CCE is 82 % for interaction at 0.1 mm from the anode, 94 % for interaction at detector mid-depth and 99 % for interaction at 0.1 mm distance from the cathode. For these reasons, gamma-ray irradiation from the cathode side and collection of the charge signal from the anode side (either continuous or pixelated) are preferred, where the electrons are mostly contributing to the signal. In semiconductor arrays of gamma-ray detectors, Barrett et al. [3] showed that the effect of hole trapping depends on the ratio of the size of the pixel ω to the detector thickness L, and that for small pixels ($\omega \ll L$) the largest contribution to the pixel signal arises from charge carriers moving to within a distance ω from the anode plane. Then, if the pixels are the anode contacts, the largest signal contribution comes from the electrons, which are less trapped than holes, thus preserving CCE and energy resolution. In the case of room-temperature semiconductors like CdTe or CdZnTe, this so-called "small-pixel effect" favors the use of detector arrays with pixels on the anode side and irradiation from the cathode (continuous electrode). However, the pixel size has not to be too small with respect to the detector thickness: in this case, spreading of the charge to adjacent pixels ("charge sharing") causes partial or total loss of spectroscopic information. Intermediate values of the aspect ratio L/ω (e.g., $L/\omega \cong 4$–5) may provide better energy resolution at energies up to 511 keV. For example, a CdTe array detector with 75 µm pixels on a 750 µm thickness ($L/\omega = 10$) has poor energy resolution (according to simulations at 60 keV [4]) and a CdTe array detector with 55 µm pixels on a 1 mm thickness ($L/\omega = 18$) has no spectroscopic resolution at all [5]; a 5 mm thick CdTe detector had an estimated energy resolution with a minimum of 4 % at 140 keV, for an aspect ratio $L/\omega = 4$ [6]. For high-aspect-ratio pixel detectors, summing up the analog signal from a sub-array of adjacent pixels should be able to recover the energy resolution, while preserving the spatial resolution.

1.3   From Semiconductor to Semi-insulating Detectors

Room-temperature operation with low leakage current is achieved with high-resistivity compound semiconductors like CdTe, semi-insulating GaAs and CdZnTe equipped with rectifying contacts as well as with ohmic contacts, thanks to their large energy bandgap >1.4 eV (Table 2.1). Since detector-grade compound semiconductor crystals (e.g., CdTe) present impurities in their growth which decrease the crystal resistivity, doping with suitable atoms during crystal growth (e.g. using Cl in the case of CdTe:Cl) is used to electrically compensate such impurities. This produces a semi-insulating electrical behavior of the crystal. For example, if all impurities are fully compensated ($n_i \cong n \cong p$), then the bulk resistivity ρ_i can be calculated as [7]:

$$\rho_i = \frac{1}{q n_i \left(\mu_e + \mu_h \right)}$$

where n_i is the intrinsic carrier concentration, n and p are equilibrium concentrations of free electrons and holes, respectively: at room-temperature, for $Cd_{0.9}Zn_{0.1}Te$, the above formula allows to derive a resistivity as large as 4×10^{10} Ωcm (i.e., one order of magnitude higher than for CdTe).

2   Semiconductor Based Imaging Detectors

2.1   Semiconductor vs. Scintillator Based Detectors

Semiconductor materials have been employed at room-temperature as substrates for X-ray and gamma-ray direct-detection imaging systems for small animal imaging (10–150 keV), since they are expected to provide a better performance, at least for some image quality parameters, than conventional indirect-detection systems, based on scintillator crystals coupled to position-sensitive light detection devices. From a schematic point of view, there is similarity between the direct and indirect detection modes (Fig. 2.4), and both can be operated at room temperature. In indirect-detection systems, gamma-rays are absorbed in a phosphor/scintillator layer and their energy is converted in a proportional number of visible or UV light photons, following primary photoelectron and electron–hole pairs creation processes. The optical photons migrate isotropically in the scintillator toward the crystal faces. Then, this optical signal is readout by a photodetector which converts the light photons into an
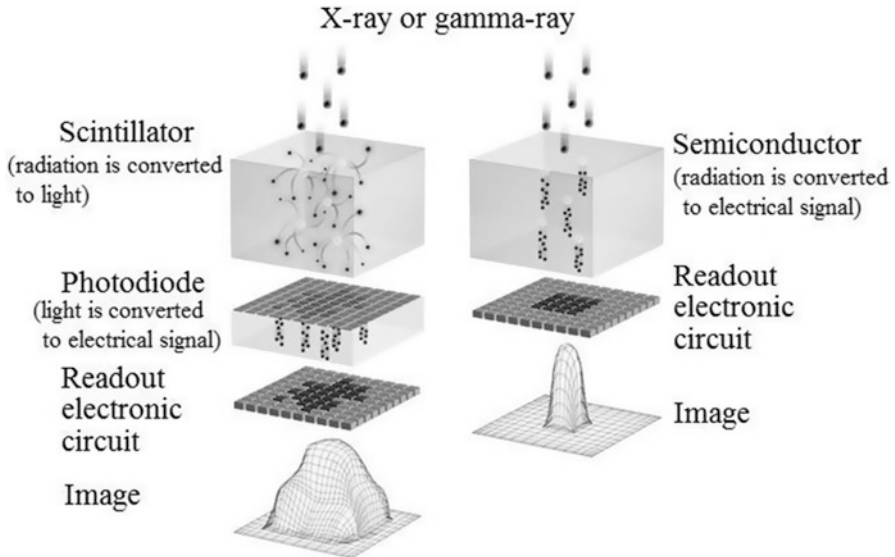
Fig. 2.4 Schematic representation of the conversion processes in a scintillator based and in a semiconductor based imaging system (adapted from [15])

intense electron current, after a large amplification. In direct-detection systems, gamma-ray photons interact in the (semiconductor) detector volume where the signal is generated as a proportional number of e–h pairs: under an intense applied electric field, these charge carriers are separated and migrate toward the corresponding electrodes, where this drift induces a current which is integrated by a charge-sensitive amplifier and converted into a voltage pulse. The photodetector + readout circuit in indirect-detection systems could be bulky (e.g. a photomultiplier tube, PMT), and this can give relatively more compactness to direct-detection systems, though the situation could also be reversed (e.g., with very compact indirect-detection systems employing a thin scintillator layer coupled to a Charge Coupled Device, CCD). Quantitative differences between the two schemes arise when considering the statistical fluctuations and the efficiency in the conversion process, the total amplification gain, the signal loss processes. All these effects determine the detector energy resolution, a spectroscopic parameter considered of importance in gamma-ray systems for human imaging as well as for small animal imaging, for isotope identification and for scatter rejection. It is of interest to examine briefly the above differences, in order to appreciate the merits of semiconductor detectors versus scintillator based detectors, for gamma-ray small animal imaging.

In the optical detection scheme with scintillators, light signal losses are present since it is not possible, in a continuous or in a pixelated scintillator crystal, to transport the scintillation light only toward the crystal side facing the photodetector surface. Indeed, this condition of light guiding toward the output surface can be realized in needle-structured scintillators like can be done for CsI:Tl, but in this case the absorption thickness is typically limited to a fraction of a millimeter, so that their use is limited to low-energy gamma-rays. The light which reaches the other scintillator faces is either absorbed (e.g. by black finishing) in order to avoid distortions in the position evaluation due to light reflections, or reflected (e.g. by reflective painting) in order to increase the light output. In addition, optical losses are present when transferring the output light signal to the photodetector window, since coupling between two optical surfaces is normally associated with lossy reflections and to light loss at the surface borders. A conservative estimate for the efficiency of light transport from the point of interaction to the photodetector window is 0.75.

Analogously, charge losses in a semiconductor detector occur in the drift process when electrons or holes are trapped in crystal defects, nonuniformities and trapping centers, so that the CCE at the electrodes is not unity, even using high-strength applied electric fields. For Si the CCE can be close to 1, but for room-temperature compound semiconductors one can assume as a conservative estimate CCE $\cong$ 0.9. In the case of a scintillator, the inefficiencies in the conversion processes—including the creation of a given number of photoelectrons at the photocathode of the light detector—determine the overall energy resolution. Fluctuations in the number of e–h pairs radiation-generated in a material are governed by a distribution whose variance is proportional, via the Fano factor F, to the average number of e–h pairs generated. Let us consider the case of NaI:Tl, where 7,500 e–h pairs are generated by a 100 keV interacting photon. These charge carrier produce, via excitation and radiative de-excitation, light photons with an efficiency of about 0.54, i.e. about

4,000 photons are generated, but of these only 3,000 reach the photocathode (75 % light collection efficiency), where they are converted to 600 photoelectrons (assuming 20 % photocathode quantum efficiency). This implies that for NaI:Tl, about 13 e–h pairs are needed to create one photoelectron in the readout photodetector. For high light yield scintillators like LaBr$_3$:Ce (6,300 photons/100 keV) and CsI:Tl (6,600 photons/100 keV) the situation is better, with about 1,000 photoelectrons generated at the photocathode, for a 100 keV interacting photon. All these factors, leading to inefficiencies in the generation of the useful photoelectron signal, are independent of each other and ultimately determine a Fano factor $F \cong 1$ (i.e., Poisson statistics applies) to the process of photoelectron generation with scintillator based detectors. On the other hand, an improved overall efficiency in the conversion from gamma-ray energy to photoelectron signal is shown by a semiconductor detector. For crystalline silicon the conversion factor is 28,000 e–h pairs/100 keV photons, and for CdTe it is 22,600 e–h pairs/100 keV photons. F at room temperature is close to 0.10 ± 0.04 for Si and for semiconductors of interest (e.g., CdTe, CdZnTe, GaAs) at gamma-ray energies of interest [8]. This means that the signal generation process has fluctuations governed by a sub-Poissonian statistical distribution. As a result, while with LaBr$_3$:Ce scintillators an energy resolution of 2.6–2.9 % at 662 keV has been reached [9], the corresponding figure for CdTe is 0.9 % [10]. At 140 keV, a continuous LaBr$_3$:Ce crystal 5-mm thick, coupled to a flat panel position-sensitive PMT, shows 9 % energy resolution. For CdZnTe, at 140 keV, a 5 mm thick detector can have an energy resolution between 3.6 % [11] and 6 % [12], the performance being dependent also on the readout electronics.

Analysis of signal conversion gain G and Fano factor F is also useful to clarify differences between indirect and direct-detection systems in terms of X-ray intrinsic detection efficiency, η, and Detective Quantum Efficiency at zero spatial frequency (DQE(0)). It can be shown (e.g., [13]) that for a direct-detection system

$$DQE(0) = \frac{\eta}{1 + \left(\dfrac{F}{G} \right)} \cong \eta$$

where the term in parentheses is close to zero since F is close to zero and G is large, for semiconductor detectors. For an indirect-detection system, the above expression is modified so as to take into account the first conversion stage (scintillator) as well as the second conversion stage from light photons to electrical charge, with corresponding parameters F_2 and G_2, so that we have

$$DQE(0) = \frac{\eta}{1 + \left(\dfrac{F_1}{G_1} \right) + \left(\dfrac{F_2}{G_1 G_2} \right)} \cong \eta.$$

The approximation holds after considering that, for scintillators, $F_1 \cong 1$, $G \gg G_1$, $G_1 \gg 1$, $G_1 G_2 \gg 1$. One can conclude that, on a quantitative basis, the $DQE(0)$ of

Table 2.2 Photon cross sections (linear attenuation coefficients) in semiconductor detectors at characteristic energies for small animal imaging

Material	Energy (keV)	Compton (cm^{-1})	Photoelectric (cm^{-1})	Total attenuation (cm^{-1})	Mean free path (mm)
Si	27.5	0.347	3.542	4.241	2.4
Si	140.5	0.310	0.020	0.350	28.6
Si	511	0.200	4.1×10^{-4}	0.202	49.5
CdTe	27.5	0.570	154.4	159.7	0.06
CdTe	140.5	0.614	3.223	4.148	2.4
CdTe	511	0.415	0.091	0.534	18.7
CdZnTe	27.5	0.570	150.3	155.5	0.06
CdZnTe	140.5	0.613	3.052	3.965	2.52
CdZnTe	511	0.413	0.086	0.525	19.0
Ge	511	0.402	0.018	0.433	23.1
BGO	511	0.509	0.396	0.963	10.4

For comparison, cross section data for a $Bi_4Ge_3O_{12}$ (BGO) scintillator crystal at 511 keV are also reported (data from [14])
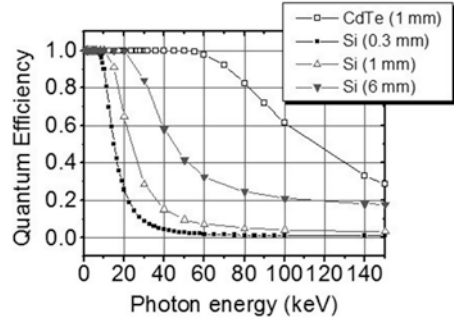
semiconductor- or scintillator-based detectors for gamma-ray imaging differ more on the basis of their intrinsic detection efficiency η rather than on their principle of operation.

The faint light signal from a scintillator for a single gamma-ray needs to be amplified with high gain (and using high voltages $\cong$ kV) by the readout photodetector (e.g., a PMT), whereas the charge (electrons or holes) from a single gamma-ray in a semiconductor can be collected with a relatively low voltage ($\cong$ 0.1 kV) and integrated with a low gain. These are additional practical advantages of the semiconductor-based systems.

2.2 Detection Efficiency of Semiconductor Detectors

For semiconductor detectors with low Z and low density (e.g., Si) (Tables 2.1 and 2.2, Fig. 2.5) η is unacceptably low for high-energy gamma-rays (e.g., 140 keV) due to their limited active thickness (typically $\leq$ 1 mm) with respect to scintillator crystal thicknesses (several mm). With this major limitation, silicon based detectors have find a role in imaging detectors for low-energy X-ray or gamma-ray applications (e.g., ^{125}I, microCT), where this mature detector technology can offer high intrinsic spatial resolution for in vivo imaging. On the other hand, edge-on irradiation geometry of thin low Z detectors permitted to reach great attenuation lengths even for high-energy for 511-keV PET imaging. Conversely, high Z, high density semiconductor based detectors (e.g., CdTe, CdZnTe) (Tables 2.1 and 2.2) offer higher absorption efficiency than scintillator based detectors of the same active thickness (Fig. 2.6). However, the active substrate thickness of those compound semiconductor detectors for direct-detection imaging applications is limited to few millimeters,

Fig. 2.5 Quantum efficiency of Si (0.3, 1 and 6 mm thickness) and CdTe (1 mm thickness) detectors (calculated with XCOM data from [14])

Fig. 2.6 Comparison of the radiation energy absorption at 150 keV in various thicknesses of scintillator and semiconductor detectors (adapted from [15])
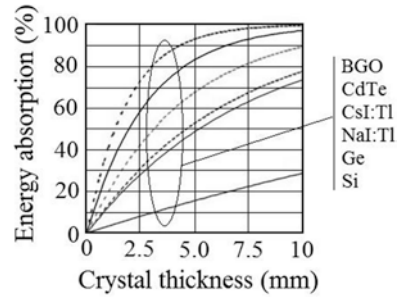
while scintillator crystals are available thick enough to provide high absorption efficiencies at high gamma-ray energies (Fig. 2.6). On the other hand, an increased thickness of the scintillator layer increases the light spread and decreases the intrinsic spatial resolution obtainable with indirect-detection systems.

For semiconductor detectors, their intrinsic spatial resolution depends on the lateral charge spread which can be controlled via electrode configuration and by application of a high electric field, since most drift charge collection occurs close to the collecting electrode. This implies that for semiconductor detectors, the pixel size can be optimized down to dimensions as small as technically feasible or down to otherwise physically limited dimensions (e.g., small pixel effect, lateral charge diffusion, charge sharing due to photon fluorescence or Compton scatter) whilst for scintillator detectors, the spatial resolution is related inversely to absorption thickness and hence to absorption efficiency.
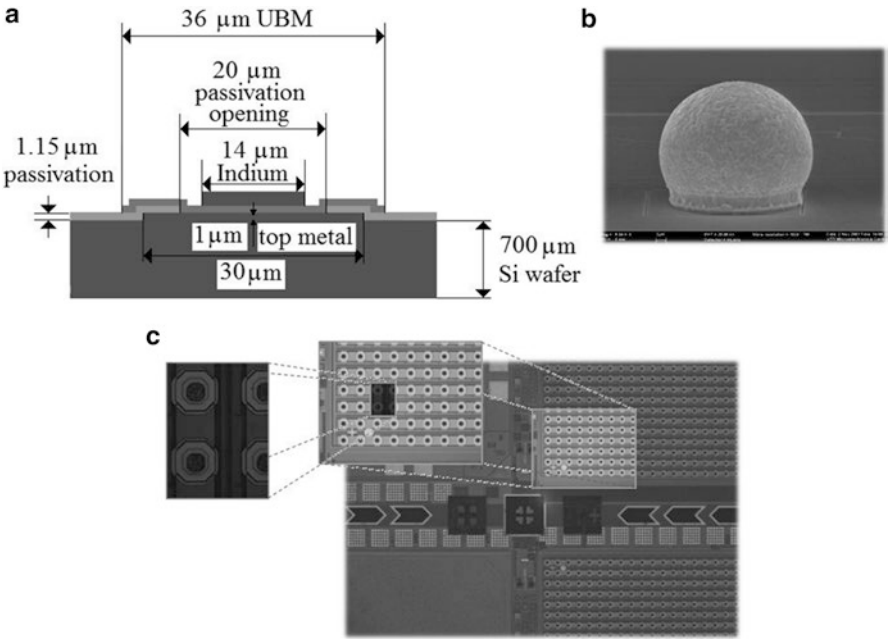
2.3 Hybrid Pixel Detectors

The term hybrid detector indicates an assembly made by coupling electrically a semiconductor X-ray or gamma-ray radiation detector (the sensor) with a microelectronic circuit for signal readout. These detectors were originally developed for
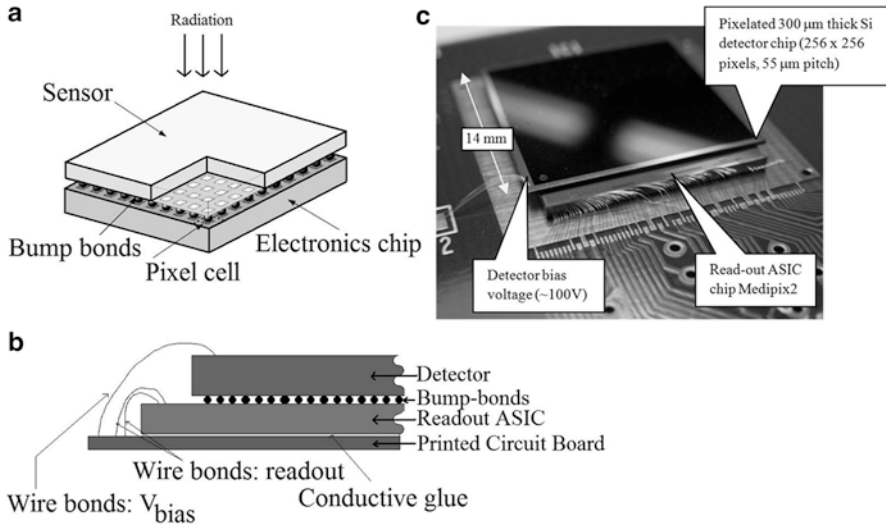
Fig. 2.7 (**a**) Scheme of a hybrid pixel detector, (**b**) scheme of detector connections, (**c**) photo of a hybrid pixel detector (Medipix2) on the printed circuit board [17]

high energy physics applications [16] (Fig. 2.7). Hence, at variance with a monolithic detector in which both the sensor and the readout functions are implemented on the same semiconductor substrate, in a hybrid detector one can optimize independently the efficiency of radiation detection and the performance of the signal processing, since the two functions are implemented on two separate semiconductor substrates which can have completely different properties. For example, the analog (micro) electronics for signal amplification and discrimination as well as the digital logic for signal processing are usually realized on low-resistivity silicon wafers, whereas the semiconductor substrate for the realization of the radiation detector can be, e.g., high-resistivity silicon, Si:Li, epitaxial GaAs, semi-insulating GaAs, CdTe, CdZnTe. These semiconductor detectors have a large energy bandgap and they usually work at room-temperature, but a moderate cooling may be employed for reducing the detector leakage current and for managing the heat load of the associated readout electronics.

For imaging applications, either a pixel geometry or a microstrip geometry have been implemented for the detector. In a hybrid pixel detector, the radiation field is sampled spatially by a 2D matrix arrangement of detector elements—pixels—and the semiconductor sensor is electrically connected pixel by pixel to a pixelated readout integrated circuit, *ad hoc* designed (Application Specific Integrated Circuit, ASIC) [18] whose pattern geometry matches that of the pixel detector. The high-density interconnection uses typically the bump-bonding technology, i.e. interposition of micro ($\cong 10$ μm) metal bumps (gold, indium, solder) between the pixel and the electronic cell [19] (Figs. 2.8 and 2.9). The production yield of bump-bonding in terms of fraction of good contacts over the detector array is usually

Fig. 2.8 Example of high-density indium bump-bonding: the Medipix2 hybrid pixel detector bump-bonded to a 700-μm thick silicon pixel detector with 55-μm-pitch pixels. (**a**) Scheme of the detector pixel, where a 36-μm square under-bump metallization (UBM) deposition is made at detector and ASIC substrates. (**b**) Scanning electron micrography of a 14 μm indium bump. (**c**) Patterning at the ASIC substrate showing, in successive magnifications, the pixel matrix array and the pixel bonding pads (courtesy of Z. Vykydal, IEAP, CTU, Prague)
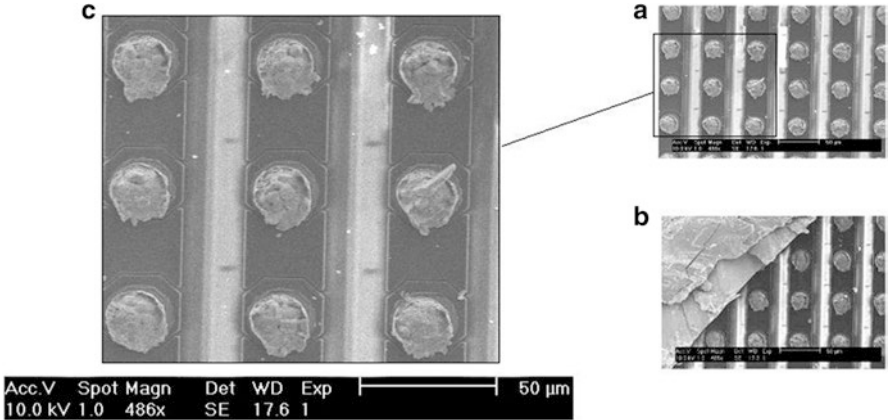
Fig. 2.9 (**a**) Scanning electron microscopy of a hybrid pixel detector, showing the indium bumps deposited with a pitch of 55 μm on the ASIC circuit. In (**b**), after hybridization, the sensor (a 1-mm thick CdTe detector) has been partially removed with a high strength force (scratched assembly). In (**c**) is a zoomed image of the bumps (courtesy of E. Manach, CEA-LIST, Saclay, France)
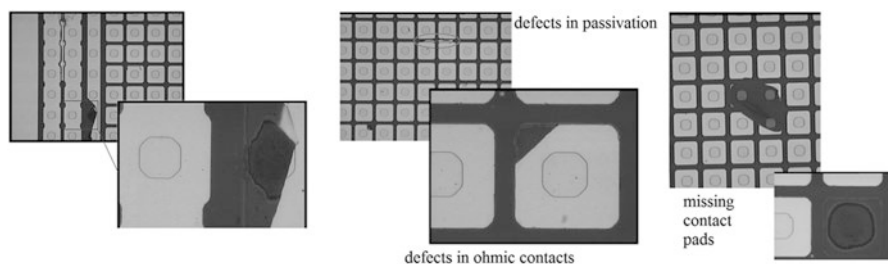
Fig. 2.10 Microphotography of a semiconductor pixel detector (CdTe, ohmic contacts) with square pixels of 55 μm pitch, prior to hybridization with the readout ASIC, showing various types of localized defects in contacts manufacturing. In the case shown the fraction of defective contacts over the matrix array was found to be only 10^{-4} (courtesy of J. Ludwig, Freiburg University, Germany)

>95 % and it may be >99.9 %; a high yield is found as well for pixel detector contact technology (Fig. 2.10).

The bump-bonding can be obtained either at high temperature (e.g., from 400 °C down to 180 °C, at the temperatures of solder bonding) or in a "cold" condition (e.g., 80 °C), as occurs in the flip-chip indium bonding technique where typically a bump is positioned on a specific bonding pad realized on both wafers (sensor and readout chip) and the two wafers are then pressed together with a force of some tens of N per chip, in order to establish mechanical and electrical connection [20]. The choice of the bonding technology depends also on the temperature requirements of the semiconductor substrate: for example, CdZnTe detector arrays are sensitive to high temperature exposures, so that hybridization is carried out in the range 60–150 °C [21]. External connection of the readout chip to the readout interface is normally done with fine pitch ultrasonic wire bonding. In this imaging detector one continuous electrode is on one side (into which the radiation is incident) and a pixelated electrode structure is on the other side (Fig. 2.11).

In a hybrid detector each pixel may correspond to the junction of a diode structure (e.g., Fig. 2.11, where a p^+n junction is formed on the pixel side), or the detector works in the photoconductive (ohmic) mode. By applying a voltage bias between the two electrode sides, an active region is formed as the depletion layer in a junction detector or as the whole semiconductor substrate volume, for ohmic detectors. The electron–hole pairs—generated by the interaction of gamma-ray photons in the detector active region—are separated by a high-strength electric field, fast enough to prevent recombination. Charge drift then occurs towards corresponding electrodes, and at the end of the drift process an induced charge (either electrons or holes, depending on the voltage polarity) can be collected at the pixel side.

The bias voltage polarity is selected so as to prefer the collection of the charge carrier type which exhibits the best transport properties in the semiconductor substrate, in the presence of charge trapping and de-trapping effects, material defects, different electron and hole mobilities, lateral charge diffusion (Fig. 2.12). The coordinate of the hit pixel(s) identifies the interaction position, while the information on
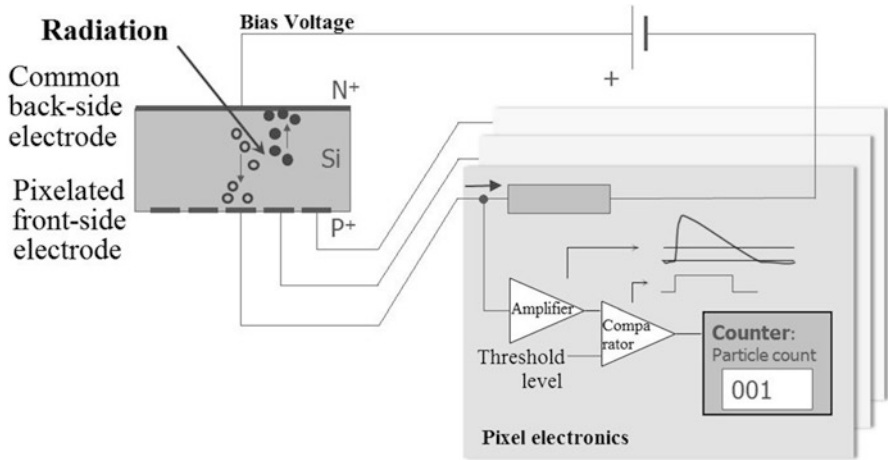
Fig. 2.11 Explaining the principle of operation of a hybrid pixel detector working in single photon counting. A single detector pixel is shown, realized as a p–n junction on a high resistivity Si substrate. The radiation-generated electron–hole pairs drift in the sensor active region under the applied electric field and the total charge reaching the pixel electrode is collected and processed by the pixel cell electronics. Either holes (as in the case depicted) or electrons can be collected, in dependence of the bias voltage polarity. The signal is passed through a charge-sensitive amplifier, its level is compared with a set threshold level and the number of interaction events (photons) is counted, for which the signal is higher than the threshold (courtesy of J. Jakubek, IEAP, CTU, Prague)
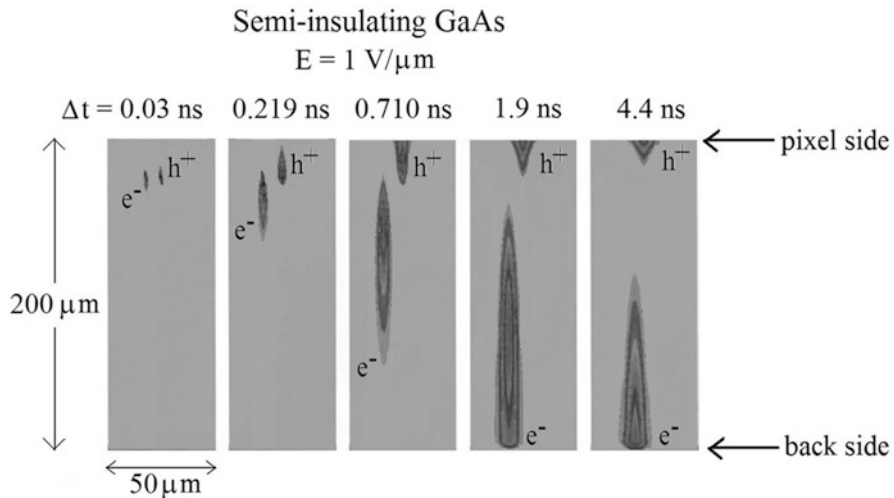
Fig. 2.12 Plot of the time evolution of the spatial distribution of 10,000 e–h pairs generated by a 42-keV photon interacting in a semi-insulating GaAs pixel detector, as determined by simulations. The 200-μm thick detector is biased at 200 V with the pixel side grounded (hole collection). The detector has 50-μm pitch pixels and the charge creation is supposed to occur at a depth of 25 μm below the surface on the pixel side, at the center between two adjacent pixels. For display convenience, the cloud of electrons (e⁻) has been slightly separated laterally with respect to the cloud of holes (h⁺). The five plots show the drift of the e⁻ and h⁺ clouds towards the collecting anode and cathode, respectively, as well as their lateral and vertical spread by electrical diffusion, at different time intervals Δt from the creation time, from 0.03 up to 4.4 ns. The grey scale of the e⁻ and h⁺ distributions indicates the charge carrier concentrations in the semiconductor bulk (data from [28], reproduced with permission)

the photon energy is given by the total collected charge, which is proportional to the deposited energy in the pixel(s). The signal due to the collection of the charge generated by a single photon or by many interacting photons is processed in each pixel electrode.

A hybrid detector can work in current mode or in photon counting mode. In single photon counting—where the pixel electronics in the readout chip is fast enough to identify and process each interacting photon during the exposure—the readout electronics of each cell may include a charge sensitive preamplifier, a single- or multiple-level discriminator and a counter or a series of counters (Fig. 2.11). A matrix-level global discriminator is normally settable for all pixels, while fine regulation of this threshold at pixel level is generally available in readout ASICs in order to compensate for small differences in the amplification of the cells. The global threshold can be regulated via the interface electronics which connects the hybrid pixel detector to the digital acquisition system. With just one discriminator level, the image matrix readout at the end of the exposure contains the total number of photons depositing, in each pixel, an energy higher than the threshold. A usual setting for this energy threshold is just above the system noise. With two discriminator thresholds available per pixel, energy windowing can be implemented for discriminating single photons on the basis of their energy, e.g. as required in gamma-ray imaging in nuclear medicine with radioactive tracers for radionuclide identification and tissue scatter rejection. With the availability of more than one counter per pixel and multiple thresholds, multi-energy ("color") single photon imaging is feasible (e.g., [22]), thus adding spectroscopic performance to the photon counting scheme.

In current mode, the collected signal at readout electrodes is due to the total induced current by all photons interacting in the detector pixel during the exposure time. This mode is typically used for high intensity radiation fields as occurs, e.g., for X-ray Computed Tomography imaging.

2.4 Microstrip Imaging Detectors

Microstrip detectors, originally developed for high energy physics and then used in medical imaging for digital radiography [23–25] and digital autoradiography [26, 27] use a semiconductor substrate (e.g. Si, CdTe, CdZnTe, GaAs, HgI$_2$) of thickness typically a fraction of a mm, on which segmented electrodes are deposited in the form of thin ($\cong$10–20 μm), long (e.g. 3–6 cm) strip metal contacts. These strips act as charge collecting electrodes for the underlying detector structures, which are either *p–n* junctions or Schottky barrier strip diodes (Fig. 2.13).

For Cd(Zn)Te, ohmic contacts as well as metal–semiconductor barriers can be realized on either or both detector sides. In very schematic and simple terms, the principle of operation of microstrip detectors is the following. For the realisation of a 1D detector, only one side of the detector (Junction side) is equipped with *n* parallel microstrips, and the opposite side is covered with a uniform contact. Under external bias, radio-induced charges (electrons and holes) drift toward their respective collecting electrode, and on the Junction side, single-polarity charge is

Double-sided silicon microstrip detector
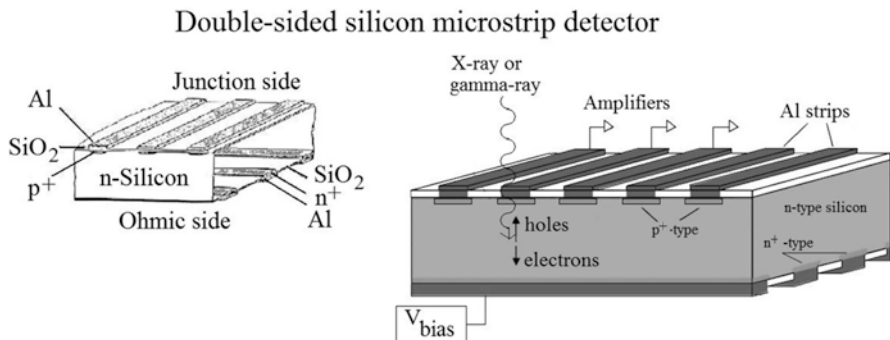
Fig. 2.13 Schematic drawings of a double-sided silicon microstrip detector, showing principle-of-operation of the device for 2D photon counting. On a (Junction) side a high-resistivity *n*-type silicon substrate, *p*+ strip are implanted to form a series of parallel junctions; *n*+ parallel strips are implanted on the back (Ohmic) side, orthogonally to the other set of strips. An aluminum contact is deposited on the strips for electrical connection to the readout circuit

collected only in one or a few adjacent strips. This gives the 1D position information of the coordinate of photon interaction. In 2D (double-sided) microstrip detectors, the back (Ohmic) contact is also equipped with *m* parallel microstrips, but orthogonal to the *n* microstrips on the junction side.

The Ohmic microstrips collect single-polarity charge carriers (electrons, in the case of reverse-biased microstrip detectors) and provide a 1D position information, too. The charge drift motion lasts a few ns, typically. By analyzing the temporal coincidence of signals on the Junction and Ohmic sides, the coordinate on one side (*X*) can be coupled (electronically on-line or via software, off-line in list-mode acquisition) with the orthogonal coordinate (*Y*) on the other side, giving a hit count in the projected (*X*, *Y*) coordinates of the photon interaction point. This allows one to reconstruct the number of interacting photons in each "pixel" of the $n \times m$ image matrix. In the case of charge sharing between adjacent microstrips, which produces above-threshold signals in (a few) close strips, the derivation of a *center-of-charge* (spatially weighted sum of strip charge signals) allows the spatial resolution to increase beyond the limit intrinsically given by the strip pitch ω (mm), up to $(2.35/\sqrt{12}) \cdot \omega$ (mm FWHM) for a uniform distribution of irradiation position between strips.

3 Imaging Requirements of SPECT and PET Small-Animal Scanners

3.1 *MicroSPECT*

^{99m}Tc and ^{125}I are the basic radionuclides in small animal SPECT imaging [1]. The latter has gained attention recently due to its low-energy X-ray (27.5 and 31.0 keV, with total emission probabilities $\cong 90$ %) and gamma-ray emissions (35.5 keV),
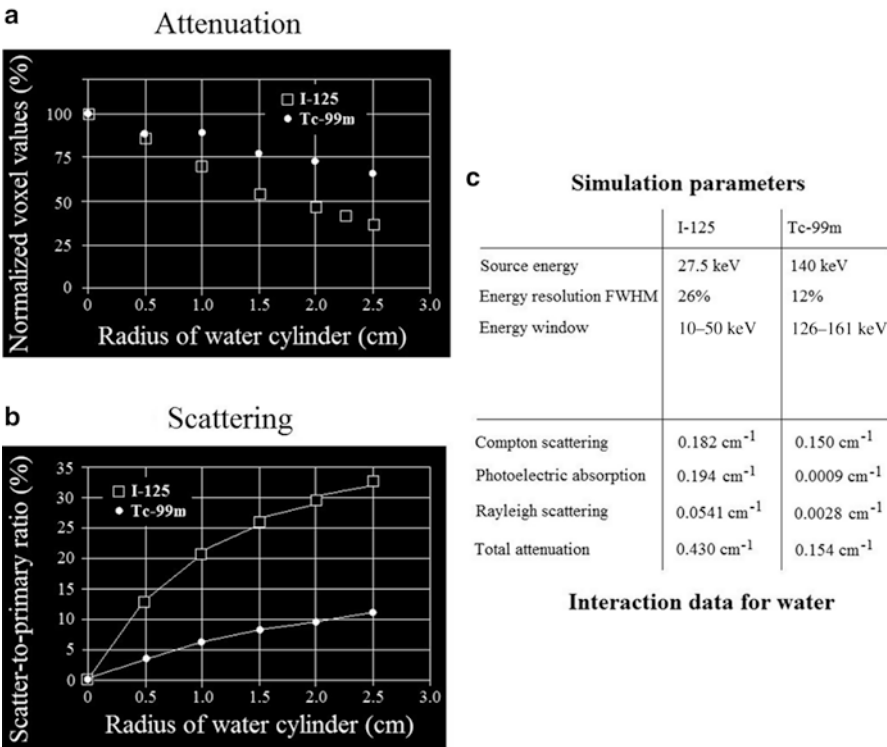
Fig. 2.14 (**a**) Simulation of the level of radioactivity for a ^{125}I source (*open squares*) or a ^{99m}Tc source (*filled squares*) as a function of the radius of a water cylinder in which the source is immersed axially. The source is a radioactive sphere of 2 mm radius. Data show that due to photon attenuation, the reconstructed radioactivity can be underestimated. (**b**) In the same geometry, the simulated scatter-to-primary ratio is significantly higher for ^{125}I than for [9m]Tc. The parameters and interaction data used in the simulation are indicated in the table in (**c**) (data from [32], reproduced with permission)

which allow to use collimators with small apertures and provide high system spatial resolution [29], but which also cope with the detection efficiency of low Z (e.g. Si:Li) [30] or thin (e.g. 1 mm CdTe) [31] semiconductor detectors. For imaging tasks and quantification of radioactive distribution in small animal organs, tissue scattering and attenuation have to be considered, since the different photon energies of the two radionuclides determine a specific different scenario. In fact, at 27.5 keV the Compton and photoelectric attenuation coefficients in water are comparable, while at 140 keV photoelectric absorption is negligible with respect to scattering (Fig. 2.14c, Table 2.3).

Monte Carlo simulations [32] showed that in a water cylinder of a few cm radius, used as a mouse phantom, the scatter-to-primary ratio (SPR) can be as high as 30 % for ^{125}I and 10 % for [99m]Tc (Fig. 2.14b). The total attenuation can determine an underestimation of the reconstructed activity at the center of the phantom by as much as $\cong$25 % (^{99m}Tc)–50 % (^{125}I) (Fig. 2.14a).

Table 2.3 Photon cross sections (linear attenuation coefficients) in water at characteristic energies for small animal imaging (data from [14])

Energy (keV)	Compton (cm^{-1})	Photoelectric (cm^{-1})	Rayleigh (cm^{-1})	Total attenuation (cm^{-1})
27.5	1.82×10^{-1}	1.94×10^{-1}	5.41×10^{-2}	4.30×10^{-1}
140.5	1.50×10^{-1}	9.05×10^{-4}	2.77×10^{-3}	1.54×10^{-1}
511	9.58×10^{-2}	1.78×10^{-5}	2.15×10^{-4}	9.60×10^{-2}
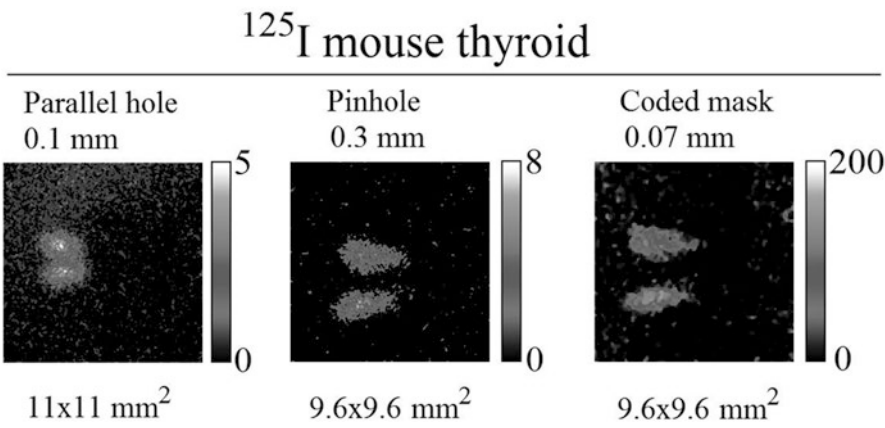
Fig. 2.15 Example of the improvement in sensitivity and a high spatial resolution provided by collimator aperture multiplexing. The mouse thyroid was imaged in vivo with ^{125}I radiotracer using the same CdTe detector (1 mm thick, 55 μm pixel pitch) coupled either to a parallel hole collimator, or to a 0.3 mm pinhole or to a coded mask with 460 apertures of 70 μm size. The exposure time per image was fixed to 20 min. The coded mask image was median filtered with a two pixel kernel

Thus, high energy resolution as a method of scatter rejection could more be of concern at low photon energies than at 140 keV, where SPR values are expected to be below 10 % in the injected mouse.

At variance with scintillator based detectors, semiconductor detectors offer good energy resolution at ^{125}I energies. However, tissue Compton discrimination at $\cong$30 keV is difficult since the scattered photon energy is too close to the primary photon energy. On the other hand, the actual influence of tissue scattering in low-count rate small animal imaging is task dependent (and observer dependent), and in imaging of small organs at a reduced Field of View (FoV) with a low injected activity, the system *sensitivity* could play a more crucial role. System sensitivity in SPECT with semiconductor detectors can be recovered by exploiting signal multiplexing (e.g., multi-pinhole apertures) and/or complex detector structures with multiple heads. As an example of the first solution, Fig. 2.15 shows a planar in vivo ^{125}I image of the mouse thyroid taken with a high resolution CdTe pixel detector, successively coupled to a parallel hole collimator with 0.1 mm holes, or to a 0.3 mm pinhole or to a coded mask with 460 holes of 70 μm size. Here, the count rate was increased by two orders of magnitude with the coded mask as compared to a 0.3 mm aperture pinhole, yet providing sub-mm spatial resolution.

A distinctive feature of semiconductor array detectors is that they could in principle be used for both SPECT and X-ray Computed Tomography (CT) small animal imaging. Indeed, in addition to working in current mode with high-flux X-ray imaging capabilities, Si, CdTe and CdZnTe based pixel detectors working in single photon counting have been produced, which can be used at the same time for low-count rate gamma-ray imaging and for high-count rate X-ray (micro)CT. An example is the CdTe gamma-ray/X-ray camera built by AJAT Oy Ltd. (Espoo, Finland) with 44×44 mm^2 sensitive area of 0.25×0.5 mm^2 pixels on a 0.75-mm thick substrate [4], or the Si [33] or CdTe [34, 35] based pixel detectors realized by the Medipix2 collaboration for X-ray imaging as well as for gamma-ray imaging [6, 36]. Those semiconductor detectors provide a useful spatial resolution for combined X-ray/gamma-ray imaging on the same small animal SPECT/CT semiconductor system.

3.2   MicroPET

There are two basic requirements for high performance small-animal PET imaging: high sensitivity and high spatial resolution; current commercial systems show 1–2 mm FWHM resolution with 2–7 % sensitivity (see Sect. 6). Spatial resolution in microPET is limited by fundamental processes of positron emission and annihilation, and improvements come from the reduction of limitations from detector geometry (detector dimensions and depth of interaction effects) and from detector physics (detector internal scatter and multiple interactions). A semiconductor based scanner can provide the solution toward sub-millimeter resolution, but improvements in sensitivity are expected as well, in a technological trend toward a target performance of detecting in vivo 0.1–1 mm^3 active volumes with 20 % sensitivity. High sensitivity results from high solid angle coverage, high detection efficiency and efficient use of all interaction events. As a typical strategy to improve sensitivity, the high density detector material should surround the animal body and its absorption thickness should be sufficient at 511 keV. A stack of thin (semiconductor) detectors is a possible solution. Gamma mean free path at 511 keV in semiconductor detectors range from 18 to 19 mm for CdTe and CZT, to 23.1 mm for Ge and 49.5 mm for Si, as opposed to 10.4 mm for a BGO crystal (Table 2.2). These figures imply that adequate sensitivity would be provided by a detector with $\cong 20$ mm absorption thickness for CdTe, CZT and Ge, and $\cong 50$ mm for Si. For adequate field coverage in mouse PET imaging with semiconductor crystals, the axial FoV could be $\cong 40$ mm and the transaxial FoV $\cong 50$ mm, with available detectors.

As described in Sect. 3.1, imaging in small animals may not require necessarily the precise determination of the energy of photons transmitted by the animal body, since the tissue interaction volume is very limited and Compton scattering in the animal body is of decreasing relevance as the photon energy increases (Table 2.3) and can be modeled. For PET energies, at 511 keV, the Compton scattering cross

section in water is 64 % of that at 140 keV, so that following the discussion related to Fig. 2.14, the scatter-to-primary ratio in a small-animal is estimated to be less than 10 % and it is less important than in clinical PET. This implies that in small animal PET imaging, photon counting (without energy information) could be a suitable acquisition strategy. As a consequence, it may not be necessary to determine the full energy peak in the spectroscopic analysis of the energy deposition by a 511-keV photon in the detector material. This signal analysis is usually performed in PET detectors where photons are counted if their energy deposit in the detector material is higher than a given high threshold (e.g., 350 keV). If Compton interaction in the detector is to be exploited for event identification, then low Z semiconductors can play a role. For example, at 511 keV, for BGO scintillator the Compton cross section is 53 % of the total attenuation coefficient whilst for Si, the Compton fraction is 99 % (Table 2.2). Moreover, in low Z materials the probability of multiple incoherent scattering is low with respect to high Z scintillator crystals of comparable thickness, this meaning that for 511-keV incident photons the fraction of single Compton interaction events is large. As a consequence, identification of the position of the (first) Compton interaction is favored and the line of flight of the two back-to-back 511 keV photons can be determined with greater accuracy than in the case of multiple interactions in the scintillator(s).

4   CdTe and CdZnTe Semiconductor Detectors

CdTe:Cl single crystals are typically grown by the Traveling Heater Method (THM) in ingots as large as 75–100 mm in diameter: this allows to cut wafers up to 50×50 mm^2 from which imaging detectors as large as 25×25 mm^2 can be derived [37], with a typical thickness of 1 mm. On such crystals, either ohmic or Schottky contacts are realized, in order to fabricate an ohmic-type (photoconductive) detector or a Schottky-type detector (Fig. 2.16).

CdTe detectors equipped with ohmic contacts show a stable response over long times and moderately good energy resolution (8–9 % at 122 keV), whereas Schottky contacts result in CdTe detectors with higher energy resolution (4–5 % at 122 keV) and count rate capabilities (Fig. 2.16). Stability of response refers to the so-called *polarization* phenomenon, observed for Schottky CdTe detectors, whereby soon after applying the detector bias voltage the energy resolution degrades and the photopeak channel decreases, this process continuing for some hours after start of functioning. Working at high bias voltages, as well as periodically interrupting the bias, helps reducing the polarization effect [37].

CdTe diode detectors show less leakage current than CdZnTe detectors of comparable thickness and this allows to use higher bias voltages: this, in turn, permits to exploit the better charge transport properties of CdTe with respect to CdZnTe which results in better energy resolution. At 22 keV, the resolution of a $3 \times 3 \times 1$ mm^3 commercial CdTe diode detector can be as good as 0.43 keV [10] (see Fig. 2.16).
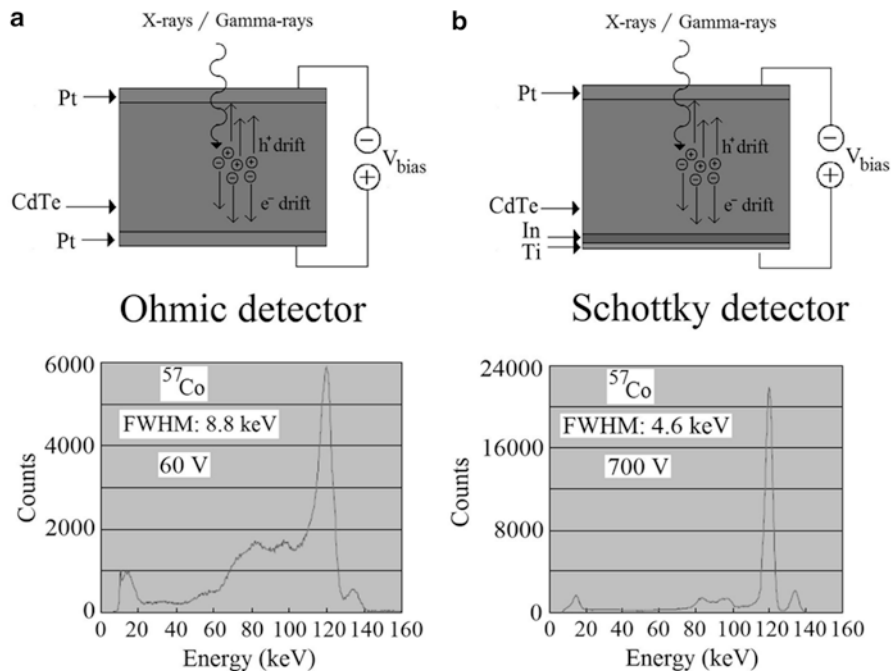
Fig. 2.16 Scheme of ohmic (**a**) a Schottky-type (**b**) CdTe detectors, and corresponding typical spectroscopic performance for 1-mm thick single-element detector of 4×4 mm^2 [37]

CdTe and CdZnTe semiconductor detectors allow to assemble compact and lightweight gamma cameras. However, since it is difficult and expensive to produce large volume semiconductor crystals with good spectroscopic quality, typical detector arrays can be realized on volumes up to 20–30 mm by side and 1–2 mm thickness. The pixel size is around 1 mm but pitch values of a fraction of a mm have been realized, and a pitch of $\cong 50$ μm is feasible. The limited sensitive area suggests to cover a large FoV and to increase system sensitivity by assembling a few detector heads around the animal. Several groups have developed compact gamma cameras based on thick CdTe or CdZnTe semiconductor detectors, for small animal planar and SPECT imaging, with single-head units as well as multiple-head detectors disposed around the animal with suitable collimators. In its turn, a single detector unit may be composed of a mosaic of small matrices detectors (e.g., 4×4): this approach allows to work with thick detector substrates (e.g., 5-mm thick) which however are typically of small-size pixels (e.g., 1.6×1.6 mm^2) [12]. Array matrices of pixel detectors based on CdTe or CdZnTe substrates can be as large as 48×48 [38] or 64×64 at 380 μm pitch [39], 120×80 at 130 μm pitch [40], 256×256 at 55 μm pitch [5] (Table 2.4).

Table 2.4 Characteristics (substrate thickness L, pixel pitch ω, aspect ratio L/ω, energy resolution $\Delta E/E$ at 122 keV) of some CdTe and CdZnTe detectors for gamma-ray imaging

| Material	L (mm)	ω (mm)	L/ω	$\Delta E/E$ (%)	References
CdTe	0.5	0.675	0.7	7.3	[41]
CdTe	0.75	0.5	1.5	3.9	[4]
CdTe	1	0.055	18.2	–	[5]
CdTe	1	0.35	2.9	2.5	[42]
CdTe	1.2	1.4	0.9	4	[43]
CdTe	1.5	0.38	3.9	–	[44]
CdTe	2	3.07	0.7	5	[45]
CdTe	5	1.4	3.6	7.8[a]	[46]
CdZnTe	2	0.38	5.3	10[a]	[38, 39, 47, 48]
CdZnTe	3	0.5	6.0	4.7	[21]
CdZnTe	5	2	2.5	3–4	[49]
CdZnTe	5	2.46	2.0	–	[50]
CdZnTe	5	2.1	2.4	4.5[a]	[51, 52]
CdZnTe	5	1.8	2.8	3.6[a]	[53]
CdZnTe	5	1.6	3.1	4.4	[54]
CdZnTe	6	4.5	1.3	6.5	[55]

[a]At 140 keV

5 Semiconductor Based SPECT Scanners for Small-Animal Imaging

In the following, some experimental scanners based on semiconductor detectors, designed for small animal SPECT imaging, will be described, with the aim of providing technical details useful for detector technology evaluation.

5.1 University of Arizona SPECT/CT System

The University of Arizona group (Center for Gamma-Ray Imaging, CGRI) has developed CdZnTe detector arrays for gamma-ray imaging with sub-millimeter pitch, with most work dedicated to the development of 380-µm-pitch 64×64 detector arrays [38, 39, 44, 47, 56, 57]. A prototype SPECT system (combined with a CT head for dual-modality SPECT/CT imaging) for small animal imaging using one such detector head has been realized in 2002 [44, 47] and is currently in use for ^{99m}Tc mouse imaging studies (Fig. 2.17). Its spatial resolution is 1–2 mm [44].

The $25 \times 25 \times 1.5$ mm^3 CdZnTe detector ([44], or $25 \times 25 \times 2$ mm^3 CdZnTe detector, [47]) is segmented on one side, via gold contact electrodes, in 330 µm square pixels with 50 µm inter-pixel gap, while a continuous gold contact is on the other

U. Arizona SPECT/CT system
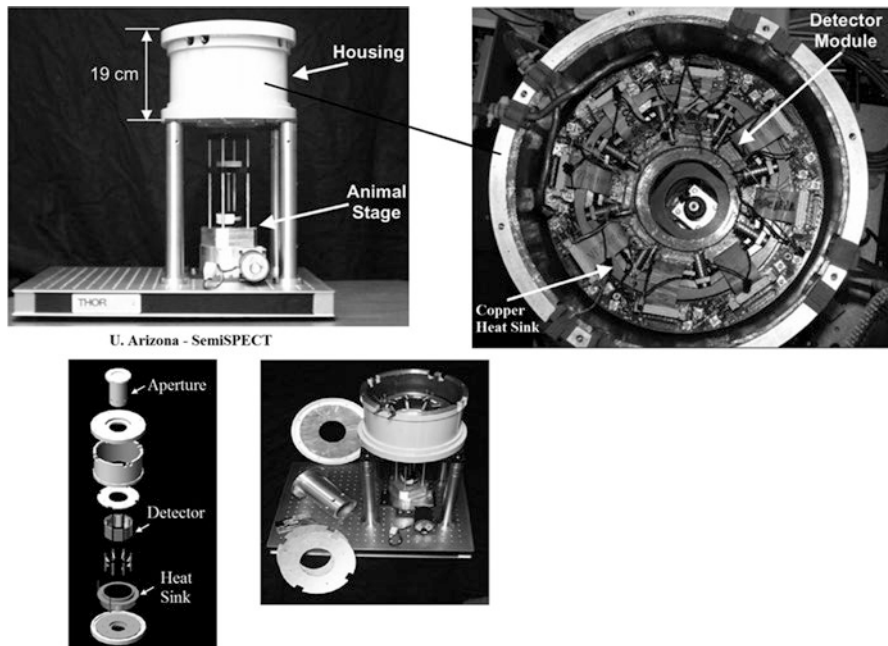

CdZnTe detector
64x64 pixels
380 μm pitch
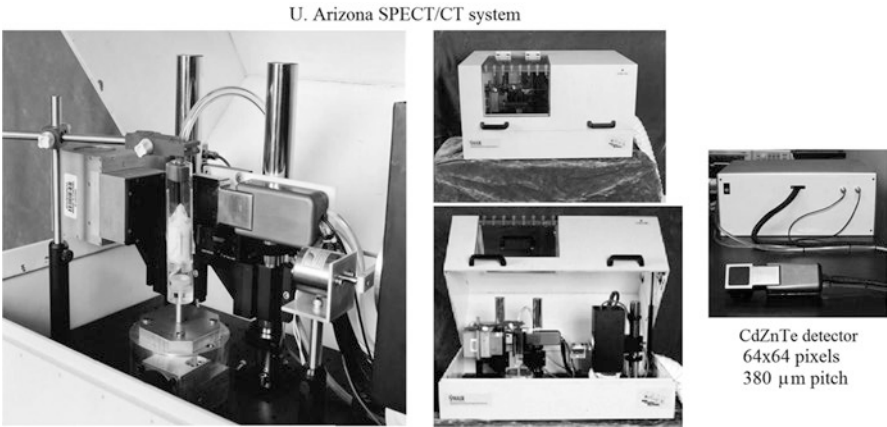
Fig. 2.17 Views of the dual modality SPECT/CT system developed by the Center for Gamma-Ray Imaging at the University of Arizona [60], based on a CdZnTe hybrid pixel detector. The detector head (*rightmost image*) is also used for spot imaging

Table 2.5 Projects done or ongoing with the small animal SPECT/CT system at U. Arizona [58]

Study	Radiotracer
Induced lung adenomas in mice	^{99m}Tc-sestamibi, glucarate, depreotide
Lymphedema in mouse models	^{99m}Tc-sulphur colloid
Detection of bone metastasis in mice	^{99m}Tc-MDP
Imaging mouse femora attached by strain gauges	^{99m}Tc-MDP
Neuroblastoma bone metastases	^{99m}Tc-MDP
Mechanism of Glucarate uptake in tumors	^{99m}Tc-glucarate
Tumor targeting of ^{99m}Tc-VIP	^{99m}Tc-VIP-Taxol
Apoptosis imaging in tumors	^{99m}Tc-C2A-GST
Dynamic SPECT imaging of mouse and rat lung	^{99m}Tc-MAA
Imaging bone metastasis in mice	^{99m}Tc-MDP
Tumor glucose uptake	^{99m}Tc-ECDG

side. The continuous electrode is at a negative −140 V potential with respect to the pixel side, where the charge collected is due to electrons. The acrylic mouse holder (a 1-in. diameter tube) is vertical. A polyacetal (Delrin™) nose piece is used to further restrain the animal and to connect to the tube for gas anesthesia. The pixel detector is indium bump-bonded to a readout ASIC. The system is mounted on an optical table and contained in an Al enclosure of $79 \times 48 \times 46$ cm^3 with 1.5 mm Pb shielding. This is a very compact imaging system whose basic design is a potential provider of reliability, ease of operation, low cost of realization and maintenance. It is in use since 2002 for various mouse imaging studies, a list of which is provided in Table 2.5.

Fig. 2.18 Views of the small animal SPECT system SemiSPECT developed by the CGRI group at the University of Arizona [48, 60]. The system is based on eight CdZnTe semiconductor detector modules each of $27 \times 27 \times 2$ mm^3 and 64×64 pixels

5.2 University of Arizona SemiSPECT System

The evolution of the combined SPECT/CT system realized by the CGRI group at U. Arizona is the SemiSPECT small animal SPECT system (Fig. 2.18) [48, 59]. This is a very complex and high performance small animal SPECT imager, which employs eight compact detector heads based on CdZnTe detectors each realized on $27 \times 27 \times \cong 2$ mm^3 substrates (64×64 pixels each, 380 µm pitch, $\cong 2$ mm thickness) biased at -180 V. This detector has 31 % detection absorption efficiency at 140 keV ± 15 % photopeak, and 54 % in the full energy range 30–200 keV. In order to reduce the leakage current, the detector heads are cooled, usually in the range from -10 to $+10$ °C, thus also removing the heat generated by the readout ASIC. The readout frame rate for each array is as large as 1,000 fps. The cylindrical FoV is 32 mm diameter $\times$ 32 mm height and the magnification at the center of the FoV is $m = 0.8$. The scanner is equipped with eight 0.5-mm aperture pinholes (0.77-mm effective diameter at 140 keV) which provide a calculated planar resolution of 1.80 mm at FoV center and a system sensitivity of 5×10^{-5}. The performance of the single detector head is 10 % energy resolution at 140 keV, obtained by summing the signal in a 3×3 array of adjacent pixels. A resolution of 1.45 mm FWHM has been reported
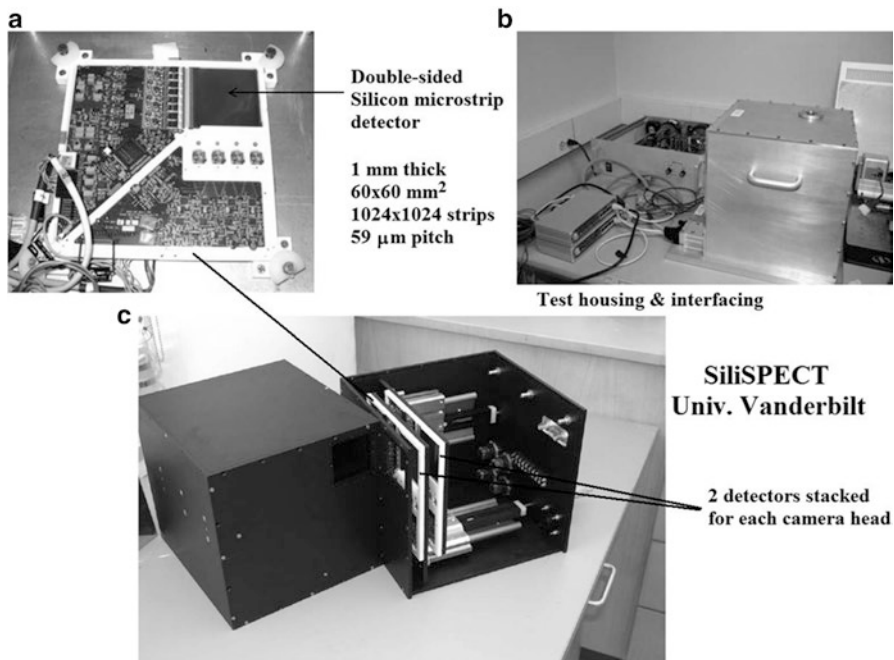
Fig. 2.19 (**a**) The detector plane of SiliSPECT, a small animal scanner based on double-sided sili-con microstrip detectors built at Vanderbilt University. The figure shows the module hosting the semiconductor detector, the readout ASICS and the data acquisition electronics. (**b**) Lab test setup for housing the detector head and for interfacing. (**c**) View of the SiliSPECT prototype, made by two heads positioned at 90°, each containing two stacked detector planes ([67, 68], reproduced with permission)

[48]. Projects ongoing on small animals with the use of SemiSPECT include a study on "human lung-cancer xenografts using ^{99m}Tc-glucarate" and "Myocardial infarc-tion in mouse heart model using ^{99m}Tc-tetrofosmin, ^{99m}Tc-glucarate" [58].

5.3   University of Vanderbilt SiliSPECT System

The group at Vanderbilt University (Nashville, TN, USA), with collaborations from University of Arizona and University of Pennsylvania, has designed and realized a small animal scanner based on double-sided silicon microstrip detectors for SPECT imaging with ^{125}I [61–66]. This is a semiconductor based, high-resolution, station-ary imager which employs focused multi-pinhole collimators for imaging small-sized objects (10–15 mm in diameter), e.g. the mouse brain, at a distance of 20–30 mm (Fig. 2.19). The SiliSPECT system is an example of a highly specialized imaging system in which apparently sub-optimal parameters (low detection

Fig. 2.20 Schematic diagram of SiliSPECT, showing the two detector heads each made of two stacked silicon microstrip detectors and coupled to a focused multi-pinhole array of small-aperture collimators (adapted from [61], reproduced with permission)
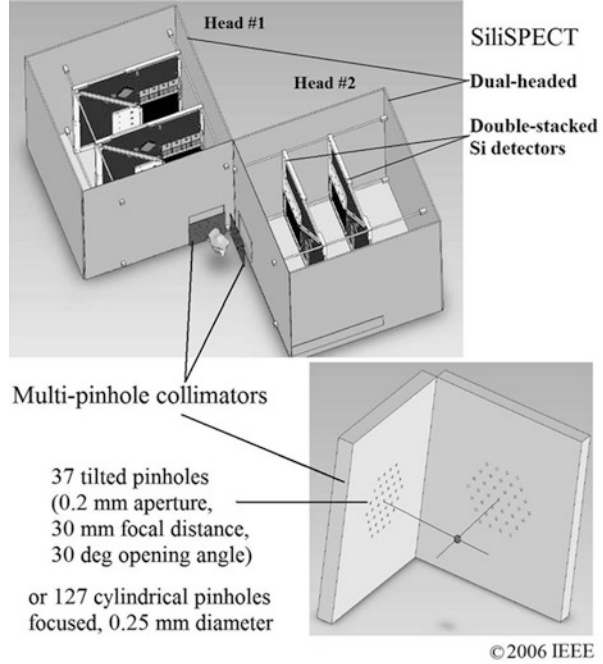
efficiency of silicon detectors, low geometric efficiency of small-aperture pinholes, small FoV, high image multiplexing) are used with advantage by focusing on specialized imaging tasks, e.g. in vivo imaging of Amyloid Beta plaques in a mouse brain with 0.1 mm resolution [66]. These systems will likely be developed in larger numbers in the future, since each animal imaging task has its own peculiarities, to be matched by specialized hardware and software solutions.

The silicon detectors of SiliSPECT have a (fully depleted) active thickness of 1 mm, starting from the first tests with a 0.3 mm thick substrate; the strip pitch is 59 μm and the detector strips are 1,024 (J side)+1,024 (Ω side), for an equivalent sensitive area of 60.4×60.4 mm^2. The use of two stacked detectors (Fig. 2.20) allows to increase the detection efficiency, which is less than 29 % at 30 keV for a single 1-mm thick Si detector (Fig. 2.5). In the list-mode acquisition and readout circuit, time stamping for coincidence processing between J-side and Ω-side microstrips is at 40 MHz clock frequency: the strip number, event time, event ADC value, are stored in two separate lists for the two detector sides, and coincident events are recovered off-line with a resolution of about 300 ns [67]. The use of a large number of close imaging apertures determines a large multiplexing on the image plane, so that image quality parameters (sensitivity, spatial resolution, noise, SNR) are not related by simple relationships to the geometrical parameters (pinhole shape, aperture, orientation and position on the collimator plane, object distance). These relationships must describe the uncertainty in the source ray direction arising from the uncertain identification of the aperture which the gamma-ray has passed

Fig. 2.21 Photo of the MediSPECT/FRI scanner for combined SPECT and planar optical imaging in small animals. The Fluorescence Reflectance Imaging part is based on a cooled monochrome CCD camera, halogen lamp with fiber optic light guides, excitation/fluorescence filters. The SPECT scanner is based on a CdTe hybrid pixel detector of the Medipix2 series, coupled to high resolution pinhole, parallel hole or coded aperture mask collimators
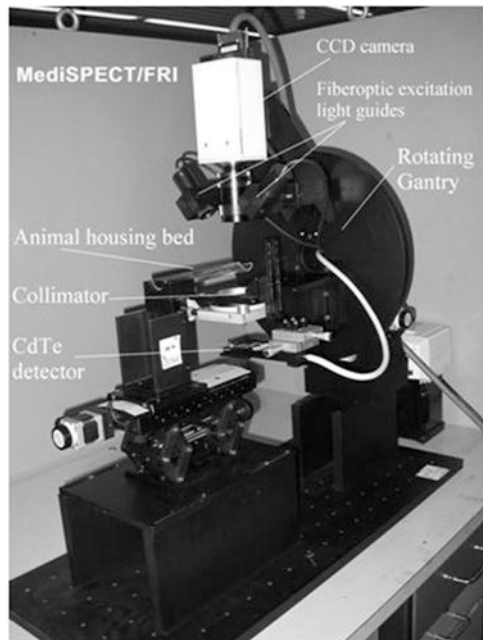

through. Moreover, imaging performance depends on the imaging task. For SiliSPECT, Monte Carlo simulations indicate that by using small acceptance angle (30°) knife-edge pinholes, or cylindrically shaped pinholes, focused toward the center of the FoV, the system sensitivity can reach 0.07–0.08 % using 127 focused pinholes of 0.25 mm diameter for each detector head [68]. The reported intrinsic resolution (59 μm) is the strip pitch [62], and the system sensitivity can be as good as 0.27 mm FWHM [61]. The SiliSPECT project is on-going, and experimental SPECT images of the mouse brain in vivo are expected.

5.4 University and INFN Napoli MediSPECT System

The MediSPECT small animal scanner is the SPECT part of a combined radionuclide/optical fluorescence reflectance imaging system (MediSPECT/FRI) realized by the University and INFN Napoli, Italy [36, 69–71] (Fig. 2.21). Most of the work has been dedicated to the development of the radionuclide subunit. MediSPECT is based on a CdTe detector (1-mm thick substrate) [34] hybridized via solder bump-bonding (AJAT, Finland) with the Medipix2 single photon counting ASIC [72] realized by the European Medipix2 collaboration [34, 73–75] (Figs. 2.22 and 2.23a). The semiconductor detector is a CdTe:Cl pixel detector fabricated on customer's specifications by ACRORAD (Japan) with the Traveling Heater Method (Fig. 2.23b).
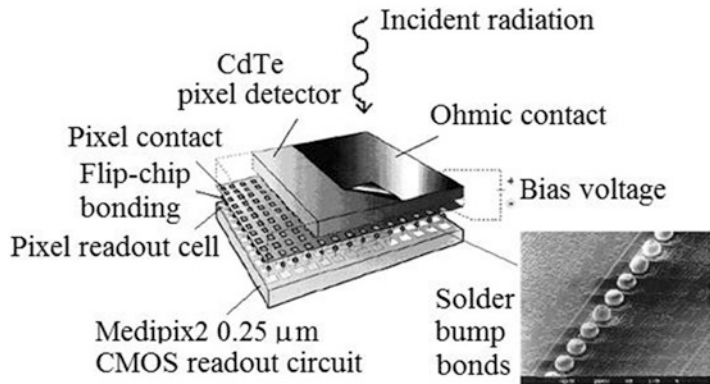
Fig. 2.22 MediSPECT is based on a hybrid pixel detector consisting of a CdTe pixel detector (1 mm thick, with ohmic contacts on both sides) and a Medipix2 readout ASIC with 55 μm square cells, as shown in this scheme
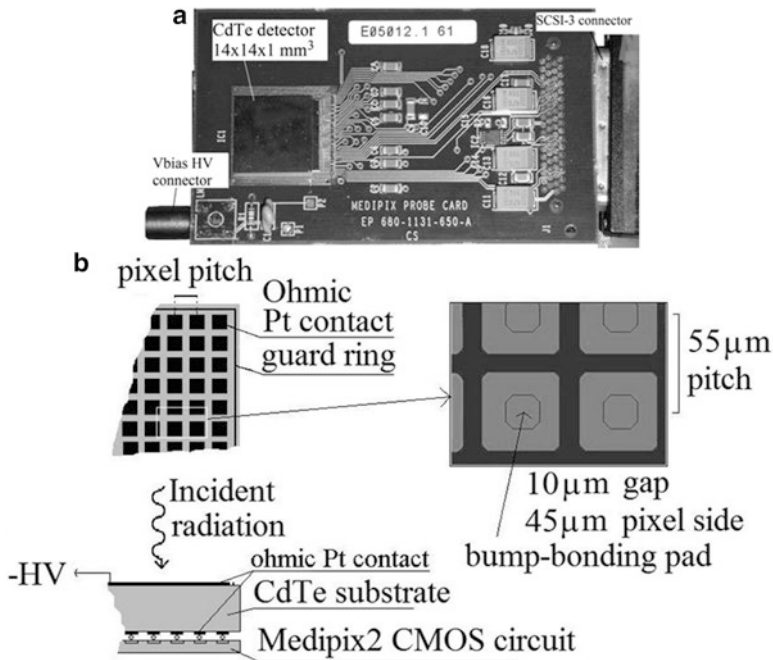

Fig. 2.23 (**a**) Printed circuit board hosting the CdTe pixel detector hybridized with the Medipix2 CMOS readout ASIC, adopted in the MediSPECT scanner. (**b**) Scheme of the CdTe pixel detector of the MediSPECT scanner

The detector has platinum ohmic contacts on both sides and its thickness is 1 mm. The contact side facing the Medipix2 readout chip side is pixelated in a matrix array of 256×256 square pixels of 45 µm side, 10 µm interpixel gap and 55 µm pitch (Fig. 2.23b), for a sensitive area of 14.08×14.08 mm^2. The detector is operated in the photoconductive mode with a bias voltage of -100 V (0.5 µA detector leakage current), determining electron collection at the pixel side. The Medipix2 cell is 55×55 µm^2 and it contains a charge sensitive preamplifier, a double threshold discriminator and a 13-bit pseudo-random counter. The Medipix2 photon counting microelectronic circuit has demonstrated a counting linearity up to 330 kHz/cm^2 [75], while the readout frame rate with the serial readout interfaces can be set typically to a maximum of a few frame per second (fps), though 50 fps have been reached with this serial interface [76] and frame rates up to 500 Hz have been reported. The dark count rate of this hybrid detector in the laboratory at room temperature is 8×10^{-3} cps/mm^2 [5]. A dedicated serial electronic interface and a software interface are used for connection to a personal computer, in order to read out the data stream from the Medipix2 ASIC and to display the $256 \times 256 \times 13$ bits raw image.

The Medipix2 readout ASIC has two detection thresholds, which permit photon energy discrimination via counting all interacting photons with energy in a window. This feature is a common basic requirement of a gamma camera, where photon energy selection around the main photopeak of the injected radionuclide emission allows to efficiently reject the Compton scattering in the tissue. Compton rejection is normally considered important for ^{99m}Tc (140 keV) imaging, due to predominance of Compton scattering over photoelectric absorption in tissue. For ^{125}I mouse imaging the low energy of the X-ray and gamma-ray emission peaks (27.5, 31.0, 35.5 keV) increases the proportion of photoelectric events in tissue, but the scatter-to-primary ratio is even higher than that at 140 keV, as shown in Sect. 3, so that in principle Compton rejection strategies are of concern in ^{125}I imaging. On the other hand, the overall image blurring effect of Compton scattering cannot be too relevant for mouse imaging, due to limited tissue absorption length (a few cm).

This is shown in Figs. 2.24 (for ^{99m}Tc) and 2.25 (for ^{125}I), where CdTe-detector spectroscopy of the radiation emitted by an injected mice or a PMMA phantom shows limited influence of Compton scattering in the sample. However, the MediSPECT CdTe hybrid pixel detector has such a fine pitch (55 µm) that a single 140-keV gamma-ray interacting in the detector volume deposits its energy in more than one pixel, due to photoelectron range and to the emission of fluorescent radiation absorbed at a small distance from the first interaction point. This "charge sharing" effect imposes a limit to the ultimate spatial resolution of fine pitch pixel detectors. Extensive studies for this specific CdTe hybrid detector [34, 77–79] permit to derive that, on the average, a single 122 keV gamma-ray deposits its energy in 2.1 detector pixels of 55 µm pitch. This implies that the energy deposition is fractioned in two or more pixels, so that spectroscopy information is not preserved in the pixel. For this reason, the Medipix2 CdTe detector employed in the MediSPECT scanner is operated with a single low-energy detection threshold of about 20 keV, thus counting all interacting photons with energy above this threshold.
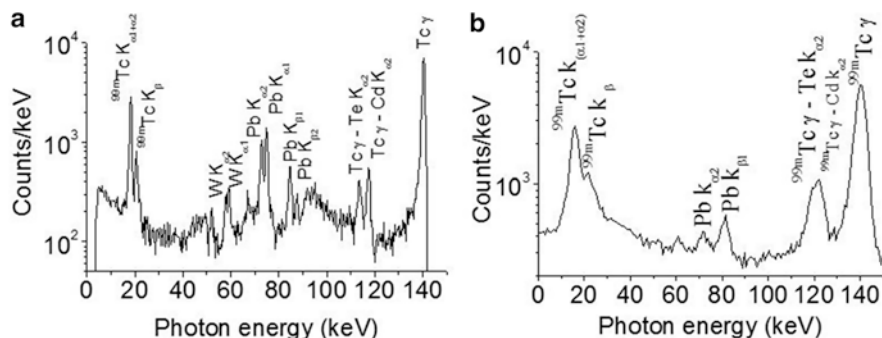
Fig. 2.24 (**a**) Pulse height spectrum of the radiation emitted from the body of a mouse injected with ^{99m}Tc radiotracer, acquired with a XR-100T-CdTe 1-mm thick detector (Amptek, Bedford, MA, USA). Photoelectric peaks are identified, arising from primary or scattered radiation from the radionuclide, from the tungsten collimators and from the lead shield around the mouse, as well as escape peaks from interaction in the CdTe detector substrate. The 140-keV photopeak has a width of 1.3 keV FWHM. (**b**) The same spectroscopy setup has been used to record the ^{99m}Tc emission from a PMMA (Lucite) phantom, so that there are 4 cm of acrylic between the source and the detector. The 140 keV photopeak has a width of 5.6 keV FWHM. The spectra have not been corrected for the energy-dependent CdTe detection efficiency
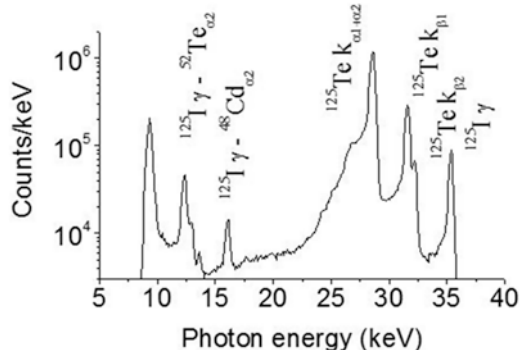

Fig. 2.25 Pulse height spectrum of the radiation emitted from a 1-mm diameter capillary source of ^{125}I inside a PMMA cylindrical phantom of 26 mm diameter, acquired with a 1-mm thick CdTe diode detector (XR-100 T-CdTe, Amptek). Main photopeaks and escape peaks are identified; the measured energy resolution is 0.42 keV at 35.5 keV. While some peak tailing is present, the effect of Compton scattering is limited and evident only on the main photopeak at 27.5 keV

For ^{125}I imaging in small animals (4–5 cm thick) this condition of spectroscopy deficit could deteriorate, according to simulations in [32], the detection performance due to the relevance of Compton scattering (see Fig. 2.14). However, in vivo ^{125}I thyroid imaging in the mouse has demonstrated a spatial resolution down to ≅0.1 mm in planar imaging [31] and sub-mm resolution in SPECT imaging (see below). Analogously, it has been observed that for ^{99m}Tc imaging in a 5-cm thick Lucite phantom the use of just a single low-energy threshold does not impair the spatial resolution (Fig. 2.26) [5], in accordance with simulations reported in [32].

Fig. 2.26 (**a**) Planar images of a ^{57}Co (122 keV) point-like radioactive source acquired with the Medipix2 CdTe hybrid pixel detector with a threshold of 20 keV, either in air or by interposing a 50 mm thick PMMA block between the detector and the source. (**b**) Radial profile of the point-like source images, indicating attenuation but limited effect of Compton scattering in 50 mm PMMA: indeed, the half-width at half maximum (indicated by the *arrows*) is practically the same for the two radial profiles
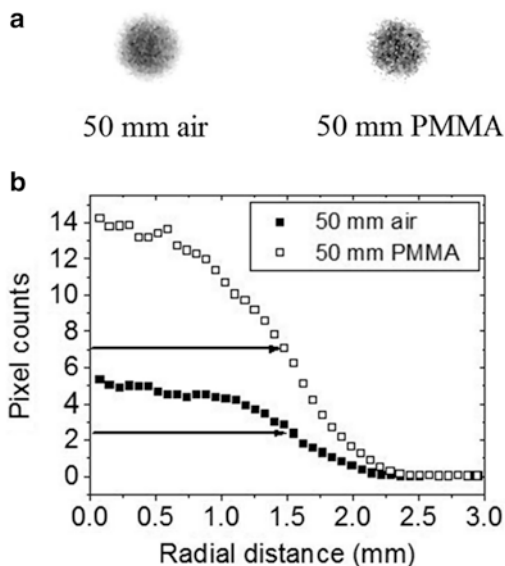
Fig. 2.27 Calculated spatial resolution and FoV in planar imaging of the CdTe detector unit of the MediSPECT scanner, equipped with a 300 μm aperture pinhole or with a NTHT coded aperture mask with 480 square holes of 70 μm side
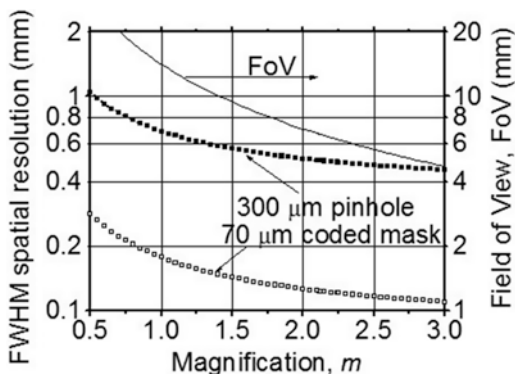
This hybrid pixel detector has a sensitive area of 1.98 cm^2, an intrinsic spatial resolution around 0.1 mm at 122 keV due to the detector pixels of 55 μm pitch, an intrinsic detection efficiency of 45 % at 122 keV [5]. Note that for this detector, the space-bandwidth-efficiency product [1] as a Figure Of Merit (FOM = detector area × detector efficiency/pixel area) at 122 keV is

$$FOM = \frac{\left(14.08 \cdot 14.08 \, \text{mm}^2\right) \cdot 0.45}{\left(0.055 \cdot 0.055 \, \text{mm}^2\right)} \cong 30000$$

a remarkable value higher than that of clinical gamma cameras ($\cong$20,000). Once coupled to high resolution pinhole or coded aperture collimators [31], a trade-off between FoV coverage and spatial resolution allows to select the proper geometrical settings for the imaging task (Fig. 2.27). However, with such a limited detector

© 2005 IEEE
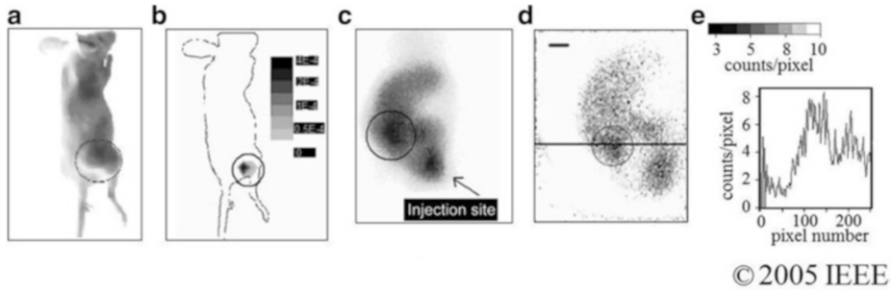
Fig. 2.28 Images of a tumor-bearing mouse (tumor area circled) injected with 74 MBq of $^{99m}TcO_4^-$ and with hematoporphyrin fluorescence marker. (**a**) white light image; (**b**) red optical fluorescence image excited in the green, superimposed on the mouse silhouette; (**c**) whole body mouse image obtained with a clinical pinhole gamma camera; (**d**) planar image (195×293 pixels, 47×71 mm², magnification=0.45, 1 mm pinhole aperture) acquired with the Medipix2 CdTe hybrid pixel detector of the MediSPECT/FRI scanner; (**e**) counts profile along the horizontal line across the tumor shown in **d**). The Medipix2 image is the result of the composition of two partially overlapped images (data from [36])

sensitive area, in order to have a sub-millimeter spatial resolution the FoV is limited to ≅20 mm or lower: thus, this scanner is best suited for specialized imaging of animal (mouse) organs, like the mouse brain, heart, thyroid, or for solid tumor implanted in the mouse body.

Preliminary combined fluorescence and radionuclide imaging tests have been reported (Fig. 2.28), but major work has been dedicated to the development of the SPECT system. The MediSPECT magnification allows to have a planar FoV ranging from 2.4 to 29 mm using pinhole collimators and from 6.3 to 24.3 mm with a coded aperture mask. The collimator unit can host different types of pure tungsten collimators (knife-edge pinhole with 0.3, 0.4 or 1 mm aperture, a parallel hole collimator with 100 µm round holes, two NTHT (No Two Holes Touching) MURA (Modified Uniformly Redundant Array) coded aperture masks with 70 or 80 µm holes).

With MediSPECT, a deep sub-millimeter system planar spatial resolution in the 0.1–0.2 mm range has been demonstrated with the usage of coded aperture mask with 70 µm holes (NTHT masks, 62×62 matrix array of open/close positions, with 460 holes). Such a hole size can be realized only in thin metal (tungsten) foils of ≅0.1 mm thickness, so that this coded mask can be used only for low-energy radionuclides as ^{125}I. This type of collimator allows to preserve a high spatial resolution (related to the single aperture size) while providing a high geometrical efficiency, up to the maximum given by the sensitivity of a pinhole of equal aperture to that of a single hole, multiplied by the number of apertures in the mask. In planar imaging, raw images produced by the overlapping of projections of the source by single apertures on the image plane (a condition known as multiplexing) are decoded off-line with a linear analysis code. In SPECT imaging, reconstruction occurs via a specific 3-D OS-EM algorithm which processes all multiplexed data from all projections at each iteration step, rather than decoding the data from each projection and then

Fig. 2.29 Volume rendered ^{125}I SPECT image of a mouse thyroid, obtained with the MediSPECT CdTe based scanner equipped with a 300 μm pinhole (magnification 1.47, ^{125}I injected activity 31.8 MBq). Acquisition parameters: 72 views at 5° steps, exposure time 1 min/view. OS-EM reconstruction parameters: 31^3 pixels with 450 μm isotropic pixel size, 15 iterations and 5 subiterations. Image FoV = $14 \times 14 \times 14$ mm^3
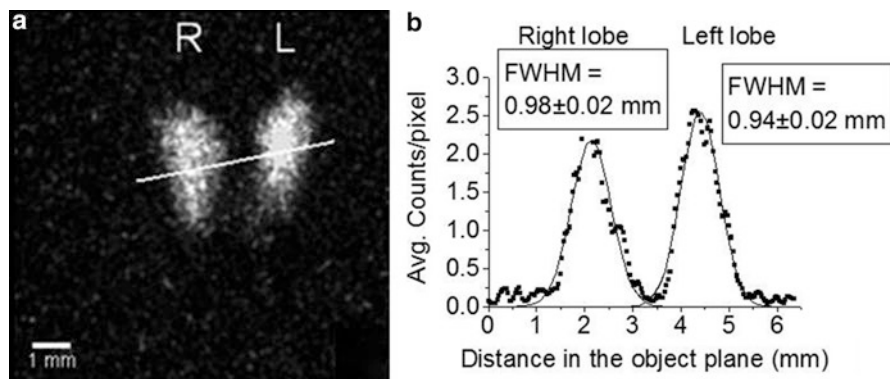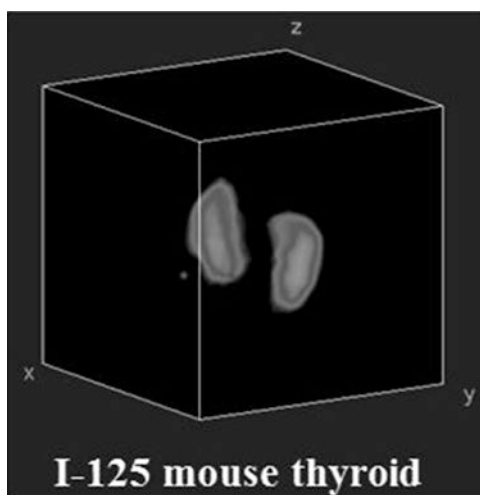

Fig. 2.30 (**a**) Planar image of an ^{125}I injected mouse thyroid taken with MediSPECT scanner equipped with a 300 μm pinhole (magnification 1.47; FoV 9.6×9.6 mm^2). The raw image has been low-pass filtered with a Gaussian kernel of two pixels FWHM. Injected activity = 31.8 MBq, acquisition time = 20 min. (**b**) The profile along the line shown on the image in **a**) indicates a size of the thyroid lobes less than 1 mm FWHM

perform reconstruction. MediSPECT has shown in in vivo mouse imaging to resolve thyroid lobes of less than 1 mm FWHM (Figs. 2.29 and 2.30). The ^{125}I sensitivity was 1.6×10^{-4} [70].

5.5 Philips Medical System's SOLSTICE System

The group at Philips Medical Systems (Cleveland, OH, USA) has developed a semiconductor gamma camera (SOLSTICE, Solid State Imager with Compact Electronics) [11, 53]. An intended application is ^{99m}Tc small animal SPECT
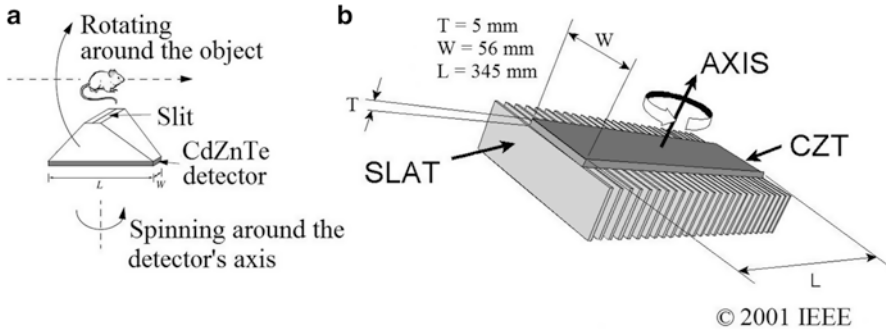
Fig. 2.31 (**a**) Acquisition geometry of the SOLSTICE small animal SPECT imager (adapted from [80], with permission). (**b**) Scheme of the CdZnTe detector and slat collimator of the SOLSTICE semiconductor gamma camera (adapted from [11], with permission)

imaging [80] (Fig. 2.31). SOLSTICE employs a series of CdZnTe detector with 5-mm-thick substrates. The SOLSTICE camera is coupled to a rotating slat collimator (Fig. 2.31a) for improved sensitivity, matching the collimator resolution with the pitch of the semiconductor detector.

The camera has a 345 mm FoV (*L* in Fig. 2.31a, b). The design requirements at 140 keV are excellent energy resolution (below 4–5 %) and high spatial resolution (a few mm). The slit camera detector axis spins around the detector's axis so that it creates 1-D projections (spinograms) of the 3-D radioactive distribution. Then, the camera is rotated around the animal to provide SPECT imaging. Essentially, this configuration requires a linear detector array in the form of a strip detector, and tests have been performed with a strip CZT detector with 192 pixels of 1.8 mm pitch [80]. Since a 1-D gamma-ray collimation is necessary, the W/Pb collimators can be made with relatively close-spaced slats (1.5 mm) matching the detector pitch, and large height (40 mm) to provide good spatial resolution. A study of CZT detector performance was made which employed sub-pixelization of the CZT detector, producing a better energy resolution. The anode side (opposite to the cathode radiation side) of each crystal (14.4×14.4 mm^2) was segmented into a matrix array of 4×8 pixels, with a pixel size of 1.5×3.3 mm^2 and a 0.3 mm inter-pixel gap.

A test of 88 CZT crystals has been reported, with negative bias voltages ranging from 275 to 420 V. The average energy resolution over the array was as good as 3.6 % at 122 keV and generally lower than the 5 % energy resolution design parameter at 140 keV [11]. The design planar spatial resolution is 5 mm FWHM at 10 cm distance. Application to small animal imaging has been reported [81] with resolution below 2.5 mm, and superior energy and spatial resolution with respect to a "conventional NaI detector" with a ultra-high-resolution parallel-hole collimator. The excellent energy resolution of the SOLSTICE/CZT camera (3.8 % at 140 keV) allowed also to perform dual isotope imaging tests with ^{99m}Tc (140 keV) and ^{123}I (159 keV) both in phantoms and in vivo on rats [81].
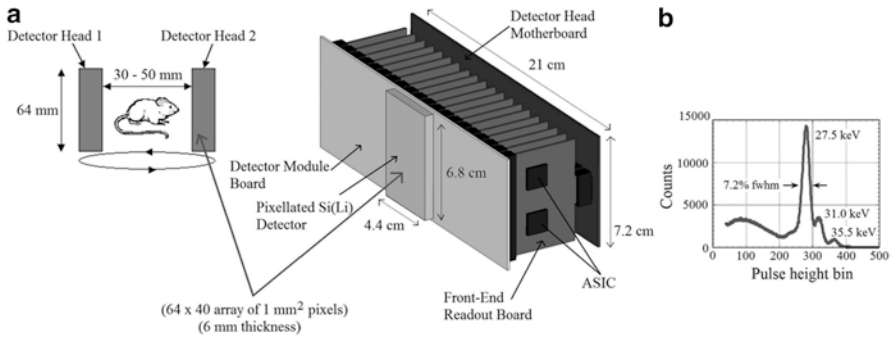
Fig. 2.32 (**a**) Scheme of the small animal ^{125}I SPECT system designed at LBNL using Si:Li pixel detectors. (**b**) Best spectroscopic performance of the Si:Li detector for [125]I (7.2 % at 27.5 keV) (adapted from [82])

5.6 LBNL Si:Li System

A high-resolution SPECT system for ^{125}I in vivo mouse imaging has been designed at Lawrence Berkeley National Laboratory, based on thick Si:Li detectors [30] (Fig. 2.32). Lithium-drifted silicon (Si:Li) crystals can be made by drifting Li in order to compensate for impurities in Si, so that an "intrinsic" Si bulk substrate can be obtained with a large thickness (e.g., 1 cm). In the LBNL design, a detector array of 64×40 square pixels of 1-mm pitch with 50–100 μm inter-pixel gap, on a 6-mm thick substrate is used, operated at room temperature since the $1 \times 1 \times 6$ mm^3 voxels have a leakage current in the order of just a few nA. The 6-mm detector thickness produces an intrinsic detection efficiency $\cong$90 % at ^{125}I energies (Fig. 2.5). Two such detector modules rotate around the animal for SPECT imaging. An energy resolution of 8.5 % FWHM at 27.5 keV has been reported (best result is 7.2 % FWHM at 27.5 keV, Fig. 2.32b) with the available discrete readout, and an energy resolution of 15 % is foreseen with the redesign of the 64-channel readout CMOS ASIC.

5.7 Gamma Medica-Ideas System

The group at Gamma Medica-Ideas (Canada/Norway/USA), in collaboration with groups at the University of California, Irvine, and Johns Hopkins University, have developed a CZT based gamma camera, compatible with Magnetic Resonance Imaging, for a small animal scanner [54]. The system is based on modules of pixelated CZT crystals, 5-mm thick, operated at −500 V bias applied to the top (non pixelated) contact, with 16×16 pixels of 1.6 mm pitch, and associated electronic readout. Each detector module is coupled to a pinhole with 0.5–2 mm aperture. By using flexible circuit boards, eight modules can be arranged in a compact "ring"

around the animal for a 30-mm FoV. A few "rings" of modules can be stacked so as to cover a larger transaxial FoV. An energy resolution of 5.4 keV at 122 keV has been reported [54].

6   Semiconductor Detectors for Small-Animal PET

There are two major issues in image quality in small animal PET: sensitivity and spatial resolution [83]. For ^{18}F imaging, scanner sensitivity currently ranges 1–7 % and spatial resolution is above 1 mm, and less than 2 mm, in state-of-the-art systems (see Fig. 2.35). However, the fundamental limiting spatial resolution in small animal PET imaging—related to positron range and non-collinearity of annihilation gamma-rays—is roughly ¼ of a mm FWHM, as estimated by summing in quadrature the contribution from ^{18}F positron range in water (0.10 mm FWHM, non Gaussian distribution) and that from photon non-collinearity (0.22 mm for a 100 mm ring diameter, Gaussian distribution) [84]. Most scanners are based on scintillator detector technology, and intrinsic spatial resolution is related to the transverse size (currently about 1 mm) of individual elements of the crystals. Further reduction in the size of the pixels in scintillator crystals is not likely to occur due to manufacturing difficulties and, in addition, a scintillator pixel with a small cross section produces a reduced light output at the readout side: this degrades significantly both energy resolution and position identification. As a consequence, in order to reach a sub-millimeter spatial resolution, several groups started dedicating efforts to the development of a new class of small animal PET scanners based on room-temperature semiconductor detectors, including CdTe and CdZnTe [85], and Si and Ge as well. In fact, for most-used PET tracers as ^{18}F and ^{11}C, simulations show that the crystal pitch is the prevalent parameter over non-collinearity and positron range effects, in determining the spatial resolution of high resolution systems. Such semiconductor detectors have been investigated for PET applications long ago (e.g., [86]), in particular for their coincidence timing properties [87, 88] which at that time was poor with respect to scintillator technology. Small animal PET involves detector rings of small diameter (several cm), and this helps reducing the influence of the detector pixel size on the intrinsic spatial resolution of the scanner.

    The intrinsic resolution of such pixel or strip detectors is ultimately limited only by the pixel pitch, which—as we have seen in the case of small animal SPECT scanners—can be well below 1 mm, thus providing the potential for an intrinsic sub-millimeter spatial resolution of semiconductor-based small animal PET scanners. Semiconductor detectors of choice, due to their high attenuation for 511 keV photons, have been considered CdTe and CdZnTe (Table 2.2). In such detectors, which are available in size of 2–3 cm by side, sufficient detection efficiency can be obtained by irradiating them by the side (planar transverse field configuration), thus exploiting a 2–3 cm attenuation length: in CdTe, this corresponds to 65–80 % intrinsic detection efficiency at 511 keV. This situation refers to gamma rays incident normally to the detector side; in this case information on the depth of

interaction (DOI) in the detector crystal is not necessary for source position determination. In the case of gamma rays incident on one of the detector faces, uncertainty in the localization of an off-axis source arises and DOI information is needed. If a stack of such semiconductor detectors is assembled for the realization of a "detector block" as the basic unit of a fixed-gantry PET ring, then the spatial resolution improvement is related to the high level of crystal segmentation, to the availability of DOI datum for each stack layer, and to a dense packing of the detector planes. Such solutions have been investigated recently in the case of CdZnTe [89], but single large CZT detectors ($15 \times 15 \times 7.5$ mm^3) with a coplanar grid electrode geometry have been tested as well [90].

In order to illustrate the technical details related to the development of a semiconductor based small animal PET scanner with ultra-high spatial resolution, in the following a few experimental realizations will be illustrated, based on Si, CdTe, CdZnTe and Ge semiconductors.

6.1   University of Ferrara SiliPET System

As described in Sect. 3.2, low Z semiconductors can be used in small-animal PET scanners where the detection strategy is identification of the position of Compton interaction in the detector. In 4-cm thick Si, the fraction of single Compton interaction events can be as large as 52 % [91]. On the basis of these considerations, the Medical Physics group at University and INFN Ferrara, Italy, proposed the realization of a small animal PET scanner (SiliPET) based on double-sided microstrip silicon detectors [92]. In SiliPET, in order to reach a suitable intrinsic detection efficiency, a stack of forty 1-mm thick Si planar detectors is used (Figs. 2.33 and 2.34), for a total absorption thickness of 40 mm Si for normally incident photons, which is close to one mean free path (49.5 mm) at 511 keV in Si (Table 2.2). Indeed, this innovative approach to photon detection in small animal PET has a number of advantages with respect to scintillator based scanners, potentially providing a very high spatial resolution (below 1 mm) coupled to high sensitivity (a few percent). In fact, Si microstrip detectors can be made large enough (e.g., 60×60 mm^2 in SiliPET) to cover a large solid angle when positioned around the animal in a box-like arrangement (Fig. 2.33a), thus increasing the scanner sensitivity. Moreover, the Si detector pitch can be small enough (e.g., 0.5 mm in SiliPET) so that the intrinsic position resolution is adequate for one-hit identification of the planar position of the (first) Compton event in a single detector plane (Fig. 2.33b): in fact, the range of Compton recoil electrons in Si from a 511-keV photon is 0.34 mm on the average and 0.57 mm at most.

The third coordinate of the position of the first interaction event is given by the position of the detector plane in the detector stack: for thin detector substrates (e.g., 1 mm in SiliPET), the resolution in this depth-of-interaction coordinate is high (with respect to a detector stack thickness of 40 mm in SiliPET). For event identification, an equivalent threshold of 50 keV in the analysis of the strip signal is set in
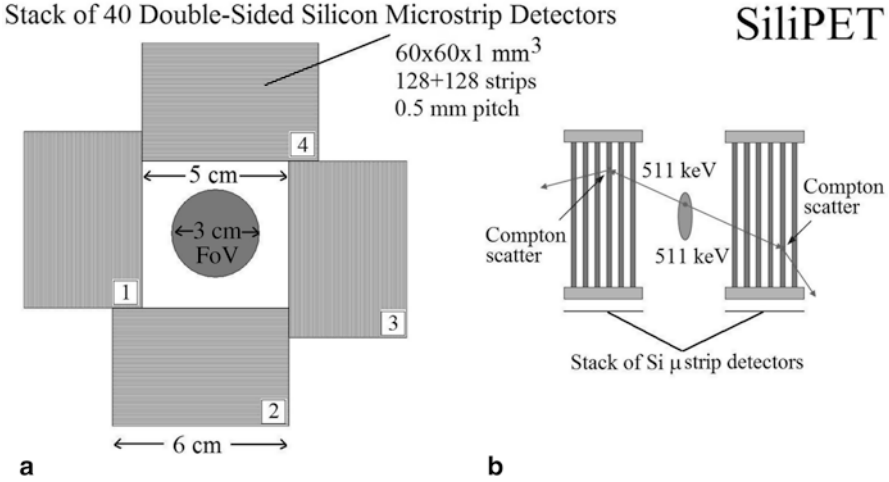
Fig. 2.33 Scheme of the SiliPET small animal PET scanner, based on a stack of double-sided microstrip silicon detectors. (**a**) Top view of the scanner geometry with the four stacks arranged box-like around the animal FoV. (**b**) Photon interaction scheme, based on the detection of Compton scatter events in two of the four stacks
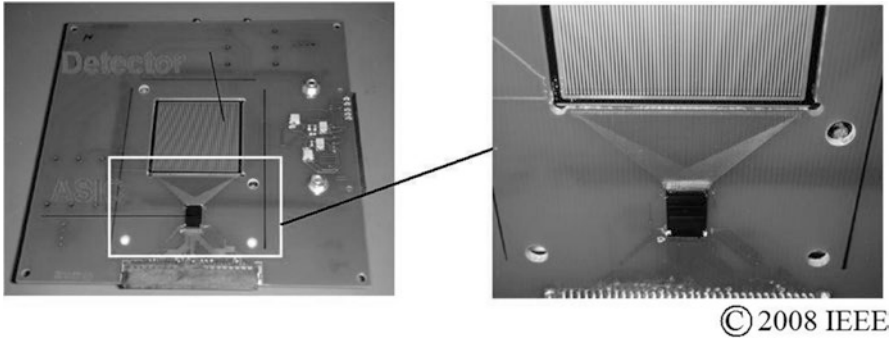
Fig. 2.34 A single detector plane (double-sided silicon strip detector, 1 mm thick, 0.5 mm pitch) of the SiliPET scanner, coupled to a commercial VATAGP2.5 128-channel analog ASIC (Ideas) for strip signal readout (adapted from [95])

the design of the SiliPET scanner. A further advantage is the reduction in complexity of the acquisition and readout electronics since no energy information is to be recorded and processed. The design and realization of a readout ASIC for fast timing measurement for the SiliPET scanner is underway at Politecnico di Milano, Italy [93]: first measurements give a time resolution of 16.5 ns [94]. Double-sided silicon strip detectors are designed and realized at ITC- Fondazione Bruno Kessler (FBK-irst), Trento, Italy, where first prototypes of 30×30 mm^2 with 0.5 mm pitch and 1 or 1.5 mm thickness have been tested [95].
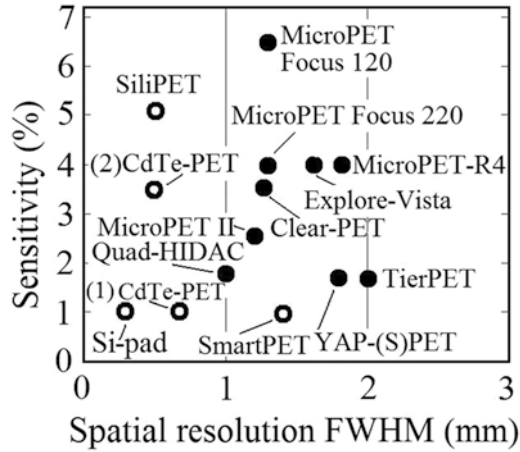
Fig. 2.35 Comparison of the performance of some scintillator based and semiconductor based small animal PET scanners, for a spatial resolution below 2 mm. CdTe-PET (*1*) refers to University of Tohoku scanner described in paragraph 6.2, CdTe-PET (*2*) refers to University of California scanner described in Sect. 6.3, and Si-pad refers to the system of the CIMA collaboration described in Sect. 6.7 (modified with inclusion of semiconductor data, from original data provided by courtesy of G. Zavattini, Ferrara University, Italy)

Overall, the above features of the design of the SiliPET scanner potentially provide (a) a high accuracy in the determination of the position of interaction, (b) a reduction of the parallax error through the determination of the depth of interaction in the detector, (c) a high solid angle coverage, and (d) a simplification in the associated readout electronics. The realization of the full SiliPET scanner is on-going and laboratory tests with prototype setups have been reported [94]. In Monte Carlo simulations for assessing its basic performance, with a point-like ^{18}F source at the center of a 3-cm diameter water phantom, SiliPET showed an intrinsic spatial resolution of 0.52 mm FWHM and a sensitivity of 5.1 % at the center of the system [91, 92]. This potential performance of SiliPET would represent a significant technological advancement in small animal PET scanners (Fig. 2.35).

6.2 University of Tohoku System

A group at Tohoku University (Sendai, Japan) proposed [96] and then developed [97, 98] a small animal PET scanner based on arrays of Schottky CdTe detectors. Initial motivations for using commercially available, thin (0.5 mm) CdTe Schottky type detectors (Pt(cathode)/CdTe/In(anode)) were their high energy resolution and low noise, when operated at high reverse bias voltages (200 V). A suitable absorption length for 511 keV gamma rays is obtained by irradiating the detectors from the side, i.e., perpendicular to the direction of the electric field inside the detector.
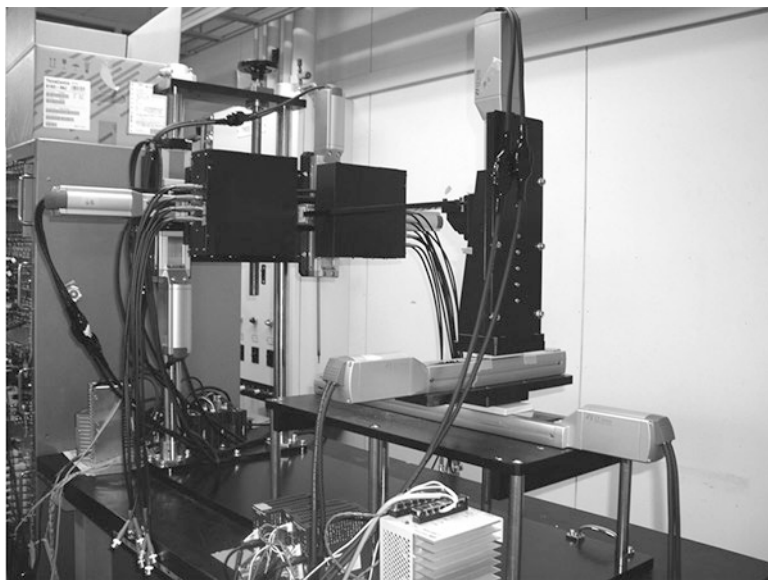
©2006 IEEE
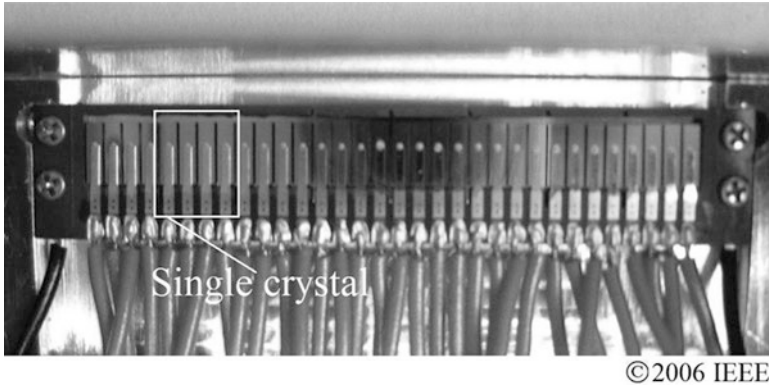
Fig. 2.36 The 32-channel CdTe detector array of the prototype University of Tohoku PET scanner, consisting of eight crystals with segmented anodes; single channels have $1.2 \times 1.15 \times 4.5$ mm^3 size (adapted from [97])

Moreover, a thin detector ($\cong 1$ mm) assures (relatively) short transit times for charge carriers to the collecting electrodes and hence, short signal rise times, which are improved by operating at applied electric fields of 300–400 V/mm or higher. For example, with a bias voltage of 400 V over a 1 mm distance between the electrodes, data in Table 2.1 for CdTe provide an estimate of 23 and 250 ns for the maximum transit times of electrons and holes, respectively.

In a preliminary report [96], two detector units were realized each one consisting of eight detectors sub-divided into two arrays of four detectors ($5.0 \times 5.0 \times 0.5$ mm^3) aligned with 2.4 mm spacing between them. The second array of four detectors is placed behind the first array, so that practically the attenuation length in the radial direction is $5.0 + 5.0$ mm: for CdTe, this total thickness provides 41 % intrinsic detection efficiency at 511 keV. Moreover, the second array is translated in 0.6 mm step laterally with respect to the first array, so as to sample the (transaxial) gap region between two detectors. Two opposing detector units, placed at 10 cm distance and readout in coincidence, with a rotating 0.6 mm diameter ^{22}Na source at the center, were able to resolve the source with 0.9 mm FWHM resolution, thus demonstrating the proof-of-principle of the sub-millimeter resolution small animal PET scanner.

The next technological step was the demonstration of array detectors with suitable detector multiplicity. An array of 32 Schottky detectors was built, consisting of eight CdTe crystals; on each crystal four detectors were produced by segmenting the readout anode electrode in four strips. This 32-channel CdTe array resulted in single channels of $1.2 \times 1.15 \times 4.5$ mm^3 size distributed over a 1.4 mm pitch (Fig. 2.36).

In a coincidence system, with a rotating 0.6 mm diameter ^{22}Na source at the center, two such detector arrays at 10 cm distance showed a time resolution of 13 ns by biasing the detector at 700 V, and a resolution of 1.0 mm [96]. Based on this detector array, a rotating gantry setup was realized (Fig. 2.37), which demonstrated an energy resolution of 3 % FWHM at 511 keV and 5 ns FWHM time resolution [97]. This

Fig. 2.37 Prototype of the University of Tohoku PET scanner with a dual head rotating gantry setup (from [97])

demonstrator showed a constant overall resolution of 1.0 mm (including 0.5 mm source diameter) with a ^{18}F phantom, with a distance between the detector heads from 50 to 150 mm, thus indicating potential performance for mouse as well as for rat imaging.

The potential of this prototype was shown in a ultra high resolution PET scanner with a fixed gantry consisting of ten detector heads arranged in a ring structure with a FoV of 64 mm diameter (transaxial) and 26 mm length (axial) (Fig. 2.38a) [98]. Full front-end and readout electronics have been realized: each one of the ten "detector buckets" consists of a detector block and ASIC amplifier unit. In the detector block there are 16 stacked detector units. Each detector unit consists of two linear arrays of 16 Schottky CdTe detectors, with one array placed in the same plane of the stack and behind the front array, shifted laterally by 0.6 mm.

Each ASIC contains 32 charge sensitive preamplifiers and is connected to the 32 signal lines from one detector unit and 16 ASICs are contained in a detector bucket (Fig. 2.38b). Ten FPGA-based digital processing boards connect to the ten detector buckets, respectively: they process above-threshold (215 keV) signals from the ASIC amplifier unit, by time-stamping the arrival of gamma rays with a 100 MHz clock (20 ns time coincidence window). The stacked detector unit contains CdTe strip detectors in two linear arrays of 19.7 mm length each, with single detectors in the array having a size of $1.1 \times 1.0 \times 5.0$ mm^3, the longer dimension being in the radial direction in the transaxial plane (Fig. 2.39). The pitch of the array is 1.2 mm. Separation between single elements in the detector array is achieved by a track of 0.1 mm width, 0.2 mm depth and 5.0 mm length on the Schottky (In/CdTe) side.
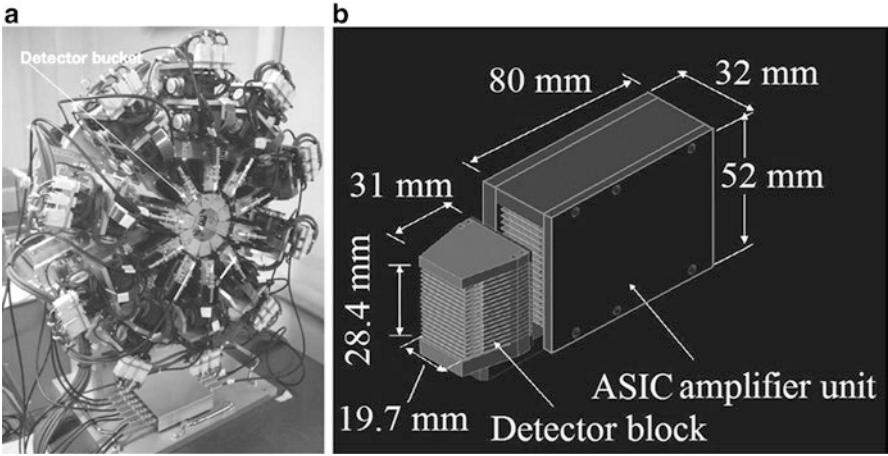
Fig. 2.38 (**a**) University of Tohoku small animal PET scanner, consisting of ten CdTe detector heads, with a FoV diameter of 64 mm. (**b**) A detector bucket (adapted from [98], reproduced with permission)

Fig. 2.39 Scheme of the dual detector arrays of 16 CdTe Schottky detectors of the University of Tohoku small animal PET scanner (adapted from [98], reproduced with permission)
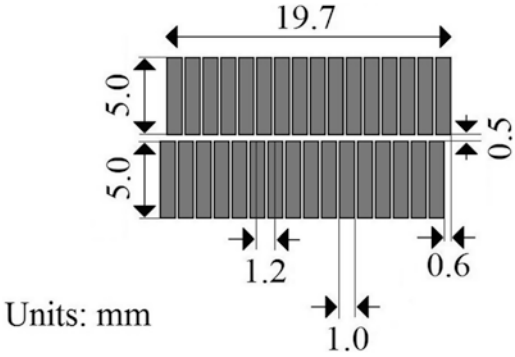
The arrangement of two detector arrays shifted by half the detector pitch allows to register up to three cross line of response in 1.2 mm transaxial distance, and to determine depth of interaction in the detector. Tests with a ^{22}Na source of 0.5 mm diameter showed a tangential resolution of 0.74 mm FWHM at the center of the FoV (Fig. 2.35); mouse and rat in vivo preliminary tests with this scanner showed high resolution performance (Fig. 2.40) [98]. The simulated sensitivity for an array of 16 layers of $1.2 \times 1.15 \times 10$ mm^3 detectors was 1 % [97].

An improvement in the position resolution of the Schottky CdTe detectors studied during the development of the University of Tohoku PET small animal scanner is represented by the realization of so-called (one-dimensional) position-sensitive CdTe detectors, i.e., Schottky devices (In/CdTe/Pt) which give the single coordinate of the interaction of the gamma rays in the direction perpendicular to the applied

**Fig. 2.40** First mouse images of the University of Tohoku small animal PET scanner: a transaxial image of a mouse brain compared to *post mortem* digital autoradiography of a brain slice of the mouse. The mouse was injected with 44.4 MBq of ^{18}F-FDG (adapted from [98], reproduced with permission)

Autoradiography   PET
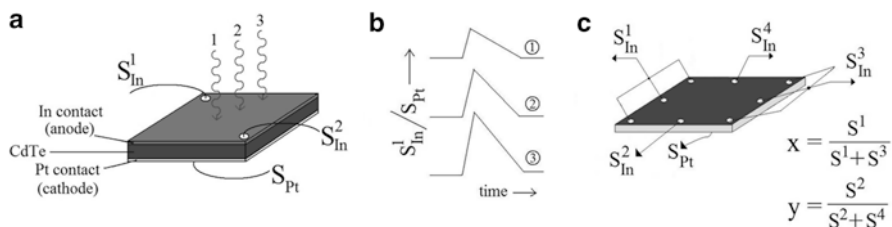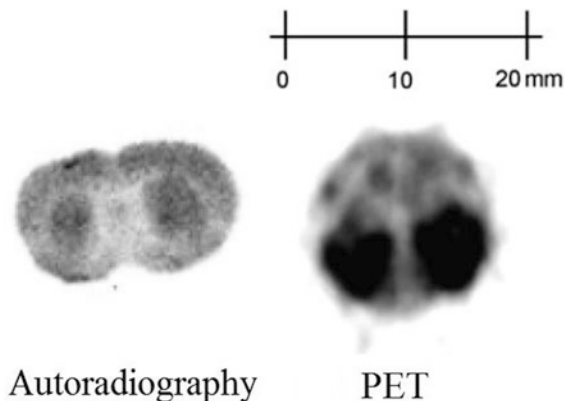
Fig. 2.41 (**a**) Schematic representation of the principle of operation of a resistive-anode Schottky CdTe detector. The ratio of the signal S^1 or S^2 from the anode side to the signal S_{Pt} from the cathode side has an amplitude (**b**) which depends on the position (e.g., 1, 2, 3) of interaction of the radiation. (**c**) By placing several readout electrodes on the In anode, the x–y coordinates of the position of interaction on the surface electrode can be recovered

electric field. It was found that if the surface resistance of the In contact is high enough, one could record a signal S_{In}/S_{Pt} as the ratio of the signal S_{In} picked up on the In anode contact to the signal S_{Pt} from the rear Pt cathode contact, whose amplitude depends on the position of the interaction of incident ionizing radiation [99] (Fig. 2.41).

The increase of the surface resistance of the In contact was obtained by decreasing the thickness of the In electrode (e.g., a thickness of 40 nm produces a resistance of 150 kΩ between two Au wires contacted at a distance of 10 mm on the surface of the In electrode), so realizing a "resistive electrode" configuration [99]. Then, the next technological step would be to place several readout electrodes on the surface of the resistive electrode, so as to derive the two-dimensional coordinates of the position of interaction of incident radiation: the University of Tohoku group has recently reported that a suitable arrangement of six readout electrode (Fig. 2.41c) is apt to recover linearly the x–y coordinates of the position of the interaction on the detector surface [100].
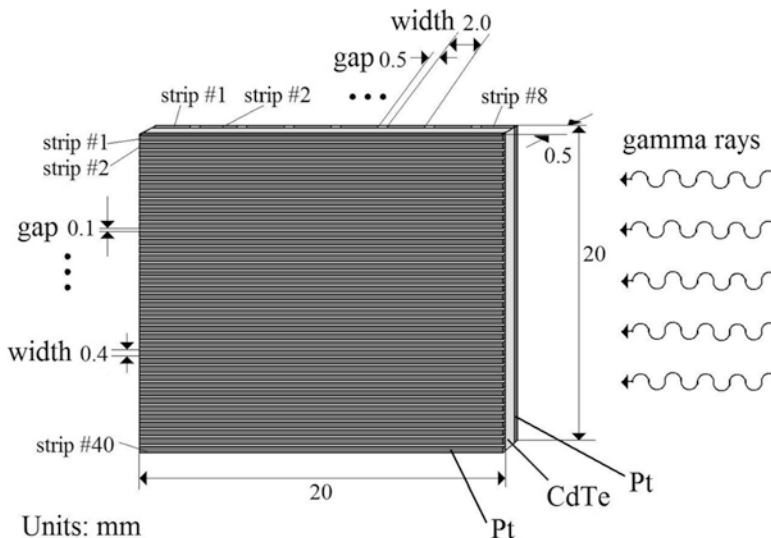
Fig. 2.42 Scheme of the double-sided CdTe strip detector employed in the University of California small animal PET scanner. The $20 \times 20 \times 0.5$ mm³ detector has 40 strips of 0.5-mm pitch along the direction of the incident gamma rays, and eight orthogonal strip of 2.5-mm pitch for providing DOI information (from data in [101])

6.3 University of California at Davis and RMD System

When irradiated from the side, i.e., orthogonally to the applied electric field determined by the bias voltage, a thin semiconductor detector can show good lateral resolution (determined by the thickness of the active substrate) and sufficient intrinsic detection efficiency (determined by the width of the detector surface). Then, 1D position sensitivity of the detector allows to obtain DOI information. In the University of Tohoku PET scanner described in the previous section, single-sided strip CdTe detectors have been used, and linear arrays of such detectors are arranged. In the case of the small animal PET scanner designed at University of California, Davis, in collaboration with Radiation Monitoring Devices, Inc. (Watertown, MA, USA), the basic detector element is a double-sided (orthogonal) CdTe strip detector of $20 \times 20 \times 0.5$ mm³ equipped with ohmic (Pt) contacts, fabricated by ACRORAD (Fig. 2.42).

In this irradiation geometry, transaxial resolution is related to the 0.5-mm pitch of the 40 contact strips of 0.4 mm width, along the direction of the incident gamma rays, and DOI information is provided by eight orthogonal strips of 2.5-mm pitch and 2.0-mm width. The absorption length of 20 mm is to be compared with the gamma mean free path of 18.7 mm for CdTe, at 511 keV (Table 2.2). Preliminary tests indicate an energy resolution of 3 % at 511 keV and a coincidence timing resolution (with respect to a LSO scintillator coupled to a PMT) of less than 11 ns down
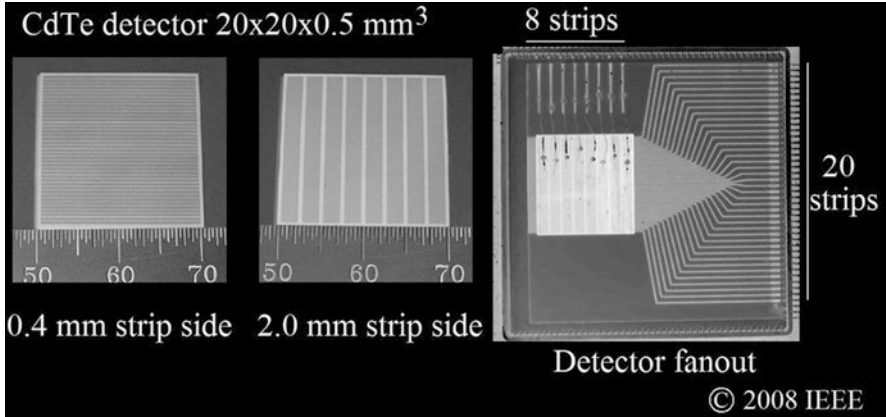
Fig. 2.43 View of the CdTe strip detector unit of the University of California small-animal PET scanner (adapted from [102])
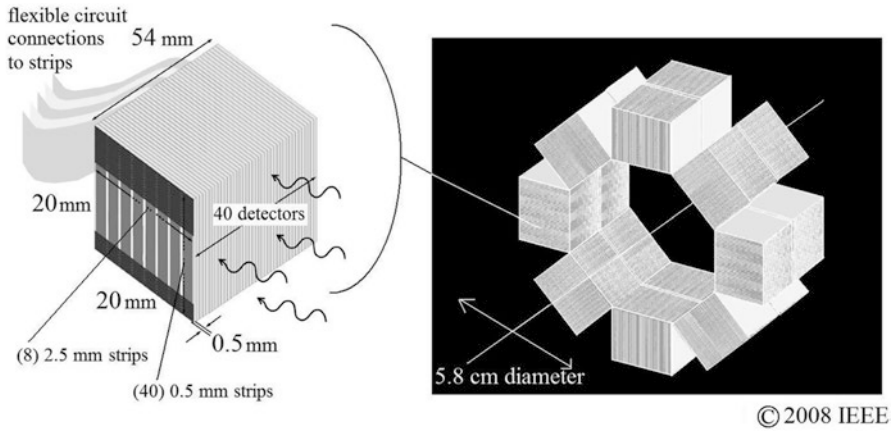
Fig. 2.44 The proposed detector block and gantry of the University of California CdTe PET small animal scanner (adapted from [102])

to 3 ns in dependence of the applied voltage bias, recorded from the 0.4-mm wide, 20-mm long strips [101] (Fig. 2.43).

Two dimensional FWHM position resolution was found to be equal to the strip pitch values (2.5, 0.5 mm, respectively). In timing coincidence measurements between two CdTe detector units, the timing resolution was 8 ns at 350 keV energy threshold [102]. A $20 \times 20 \times 24$ mm^3 detector block was designed, made by stacking 40 such detector elements, and two such blocks are coupled for increasing the axial FoV, in a gantry arrangement of 16 detector blocks with an inner ring diameter of 5.8 cm (Fig. 2.44). Such a scanner has potential for 3.4 % sensitivity [102]
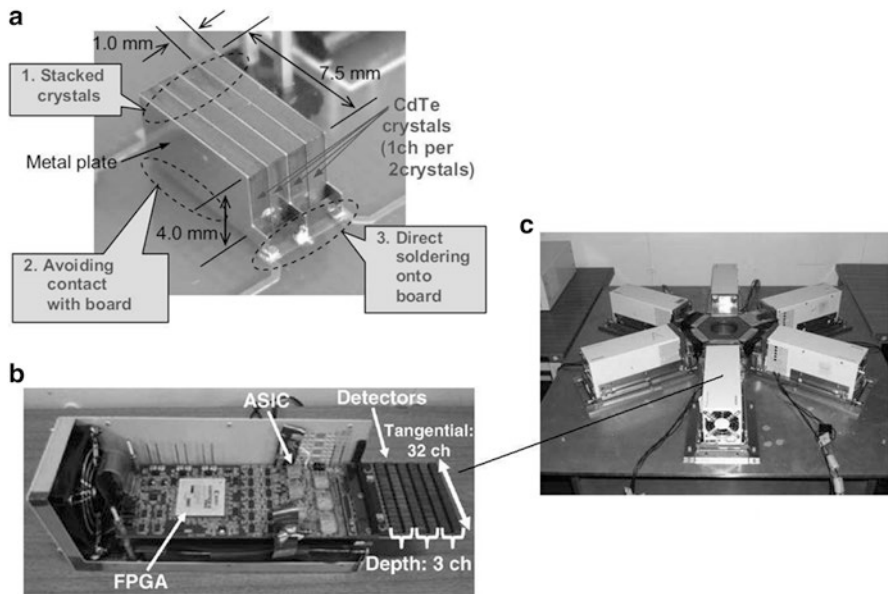
Fig. 2.45 (**a**) The CdTe detector module consisting of four crystals and two channels, (**b**) the detector unit with 32×3 detector channels and (**c**) the single slice ring (82 mm inner diameter) of the prototype PET scanner developed by Hitachi Ltd. and University of Hokkaido (from [103, 104])

(Fig. 2.35). Given its complexity, it represents a major technological challenge for detector assembling, interconnection, data acquisition and processing. However these challenges compete with the major potential of semiconductor detectors vs. scintillator detectors for sub-millimeter spatial resolution and high sensitivity in small animal PET imaging.

6.4   Hitachi and University of Hokkaido System

In view of the realization of a 3D PET scanner for human brain imaging using CdTe detectors, a group at Hitachi Ltd. (Ibaraki, Japan) in collaboration with Hokkaido University (Sapporo, Japan) has made a single-slice prototype of a PET scanner based on six stacks of CdTe detectors [103], useful for small animal, e.g., rat imaging. Each detector module is a stack of four crystals, each of size $1.0 \times 7.5 \times 4.0$ mm^3, and 96 detector modules are arranged in six detector units in a single slice ring (Fig. 2.45).

A single detector channel is composed of two adjacent crystals with 2.3 mm pitch ($1 + 1$ mm thickness $+ 0.3$ mm gap) in the tangential direction, and two crystals with 17.5 mm pitch in the radial direction ($7.5 + 7.5$ mm
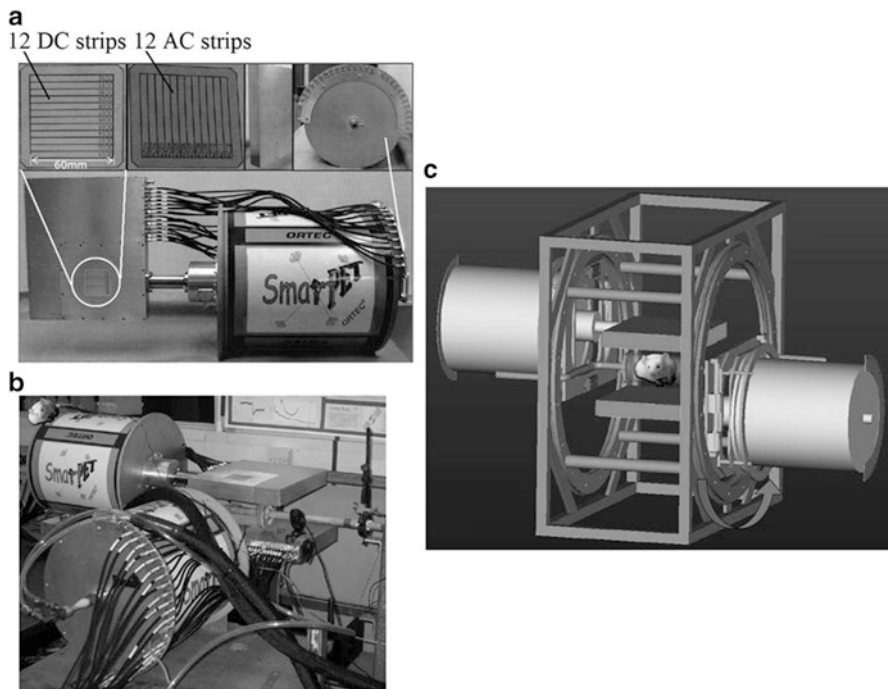
Fig. 2.46 (**a**) The HPGe planar detector module consisting of a double-sided strip detector $(60 \times 60 \times 20 \text{ mm}^3)$ with $12 + 12$ orthogonal strips of 5-mm pitch, (**b**) the two detector heads and (**c**) the dual-head rotating gantry of SmartPET, the small animal PET demonstrator developed by University of Liverpool. The large cylinders are the 72 h dewars for cryogenic cooling of the detectors with liquid nitrogen (from [108])

thickness + 2.5 mm gap). Under tests, the timing resolution was 6.0–6.8 ns FWHM (450 keV threshold), the energy resolution was 4.1–5.4 % FWHM and the spatial resolution was 2.6 mm FWHM.

6.5 University of Liverpool SmartPET System

In their analysis of image blurring in scintillator based PET systems for human imaging, caused by scattering of one or both of the collinear 511 keV gamma rays, the group at University of Liverpool identified the need for a very high energy resolution for rejection of background events and improved image quality. Hence, they proposed [105, 106] to use High Purity Germanium (HPGe) planar detectors for PET imaging, due to their excellent spectroscopic properties, and their detection properties approaching that of CdTe at 511 keV (Tables 2.1 and 2.2). In order to investigate this technology, in the framework of a 5-year hardware/software study started in 2003, they built a demonstrator that works as a small animal PET scanner (SmartPET) (Fig. 2.46),

but that has been used also in Compton imaging configuration [107]. The SmartPET prototype is a dual head, rotating gantry system based on a pair of double-sided high purity Germanium strip detectors. The p-type Ge crystals are $74 \times 74 \times 20$ mm^3 each with an active volume of $60 \times 60 \times 20$ mm^3; a 7 mm wide guard ring surrounds the active surface on the two detector surface. The outer contacts are segmented into 12 strips per side with a pitch of 5 mm, thus defining equivalent voxels of $5 \times 5 \times 20$ mm^3. The strips are defined by p$^+$ AC coupled contacts (49.82 mm wide and 0.18 mm inter-strip gap) on one side, and orthogonal DC coupled n$^+$ contacts (49.70-mm wide and 0.30 mm inter-strip gap) on the opposite side (Fig. 2.46a) The separation between the two detector planes is 130 mm (Fig. 2.46b, c); the detectors are operated at −1,800 V bias. The raw spatial resolution of such a detector would be equal to the (equivalent) detector pixel, i.e. 5 mm on the detector planes and 20 mm in the direction perpendicular to the scanner axis, implying no DOI information. On the other hand, Pulse Shape Analysis (PSA) of the charge signals on the AC and DC strips allows to recover a higher intrinsic spatial resolution [109]. The improvement in lateral spatial resolution using PSA techniques derives from the analysis of the charge signals induced, by the e–h carriers drift motion, both on the hit strip and on adjacent strips. When a pixel strip is hit by an interacting gamma-ray, the area under the signal waveforms in the left-side and right-side strips varies in dependence of the actual position of interaction across the 5-mm wide strip: by evaluating an asymmetry parameter between the two area values, a lateral position resolution of 1 mm has been demonstrated [109]. As regards DOI information, an event-by-event analysis of the pulse shape rise time—which depends on the depth of interaction below the detector surface—showed that, away from the detector edges, it depends linearly on the event DOI, thus permitting to reconstruct the interaction depth [110]. The rise time distribution of single-pixel events could be divided into five regions, thus permitting a coarse resolution of about 4 mm along the 20 mm detector depth [109].

The timing resolution was approximately 10 ns [106, 111], and initial tests at 122 keV indicated an energy resolution less than 1.5 keV FWHM for the SmartPET detectors [106], though the excellent energy discrimination of the HPGe detectors seemed not play a determinant role in the overall performance of the scanner, in subsequent works of the Liverpool group. As regards the detection sensitivity, measured for a ^{22}Na source at the center of the FoV and without full-energy event recover analysis, the dual-head SmartPET prototype showed an absolute sensitivity of 0.99 %; this value reduces to 0.12 % by limiting the data analysis to single pixel events, and to 0.001 % to single pixel photopeak events [112]. This demonstrates that for a significant sensitivity, all interaction events had to be considered. By accepting, in the event selection stage of data analysis, all events where one or both detector heads recorded either one or two strip hits per interaction, the SmartPET prototype showed a resolution of 1.4 mm FWHM with a statistical reconstruction and of 2.7 mm FWHM with an analytical reconstruction algorithm, for a point-like ^{22}Na source at the center of the FoV.
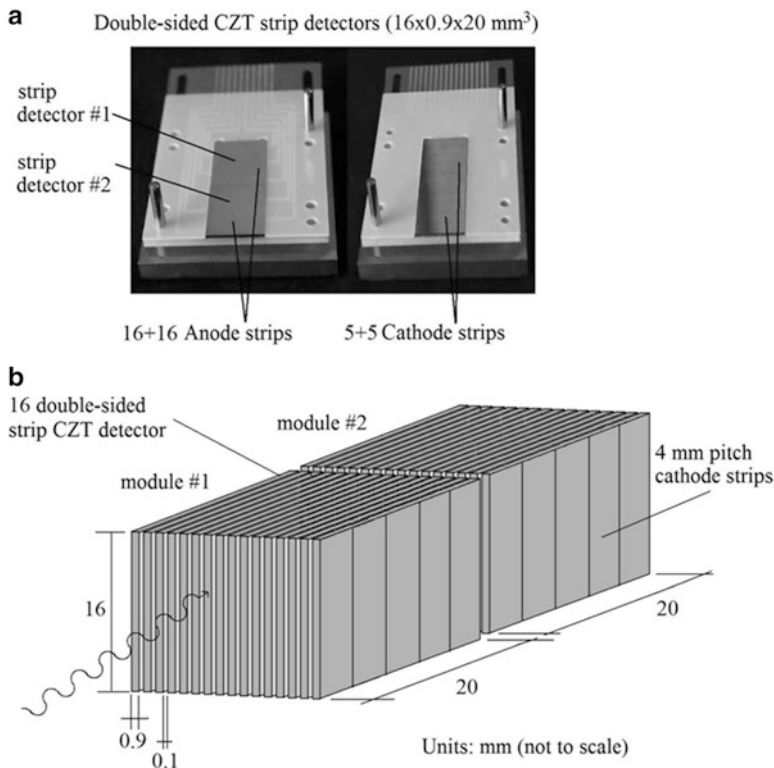
Fig. 2.47 (**a**) View of anode and cathode sides of CZT orthogonal strip detectors fabricated by CEA-Leti for microPET. Two detectors are placed in the same plane one behind the other, in order to double the attenuation thickness to 40 mm for gamma-rays incident edge-on along the detector length. (**b**) Sixteen detector planes are stacked with a 0.1 mm plastic sheet in between, for realizing a detector block of $16 \times 16 \times 40$ mm^3 active volume (adapted from [114])

6.6 CEA-Leti CZT System

The group at CEA-Leti (Grenoble, France) has been pursuing the realization of a PET scanner based on CdZnTe detectors. The higher resistivity and the absence of polarization effects with respect to CdTe, motivated their choice of CZT as a suitable material for their PET prototype. First experimental tests have been shown with detector modules consisting of arrays of double-sided CZT strip detectors 0.9-mm thick, irradiated edge-on along their length, with 20 mm length and 16×16 mm^2 faces, with 1 mm pitch on the anode side and 4-mm pitch on the cathode side (for DOI measurement), respectively (Fig. 2.47a) [113]. The detector planes are made by two 20-mm long arrays, put one behind the other for 40 mm total attenuation thickness, each array being made of 16 $16 \times 20 \times 0.9$ mm^3 strip detectors with a separating polyimide sheet of 0.1 mm thickness (Fig. 2.47b). Coincidence timing tests

Si pad detector   16x32 array of 1.4x1.4 mm^2 pads on 1 mm thick Si substrate
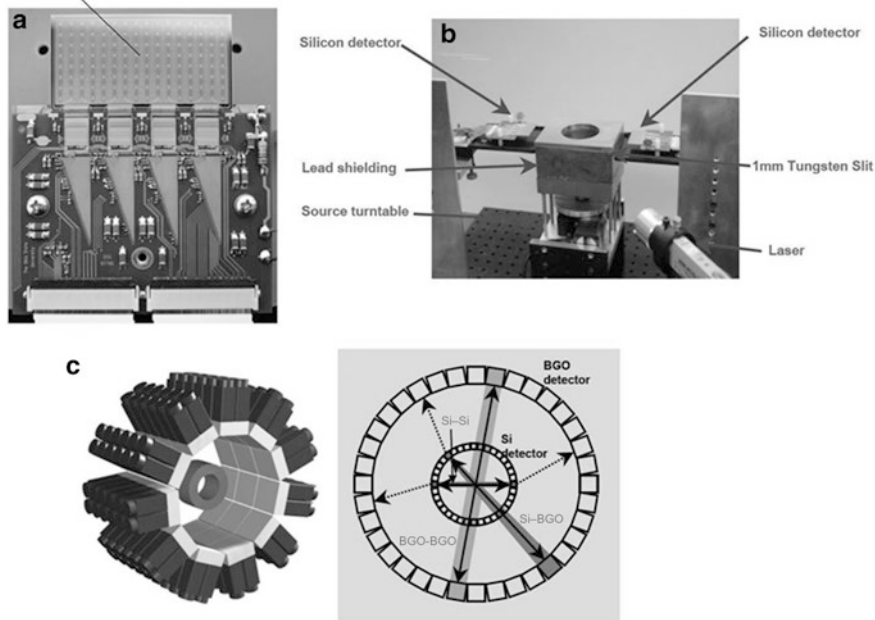
Fig. 2.48 The CIMA collaboration has designed a small animal PET scanner (**c**) based on a conventional BGO ring detector with an internal ring of silicon pad detector. One such detector is shown in (**a**) while in (**b**) is a photo of the dual head prototype setup of the silicon pad detectors, where the laser is used for detector alignment [117]

in planar geometry with two CZT detectors gave a resolution of 2.6 ns FWHM, and with a CZT detector and a fast BaF$_2$ scintillator gave 2.1 ns FWHM on anodic signals at 500 V bias voltage [89].

6.7 CIMA Collaboration Si Pad System

The Computer Imaging for Medical Applications (CIMA) collaboration [114] has developed a dual head prototype of a silicon detector small animal PET scanner, to be used as a high-resolution insert for a conventional scintillator based PET scanner [115]. The silicon detector ring, internal to the BGO detector ring (Fig. 2.48c), is made of 1-mm thick Si diode detectors (p$^+$–n junction at pad contacts and n–n$^+$ contact on the back) contacted with a 32×16 array of 512 pads (Fig. 2.48a). A double metal layer is used for routing pad connections to the bonding pads to commercial 128-channel readout ASICs. The inner ring is designed to Compton scatter 511 keV photons: in fact, most events are either direct absorption interactions in the scintillators, or single Compton scatter events in the low Z semiconductor detector followed by absorption in the scintillator detector (Fig. 2.48c). This

introduces the distinction between Si–Si interactions, Si–BGO interactions and BGO–BGO coincident interactions. The single scattering event in the Si detector can be localized with high spatial resolution due to the short range of the Compton recoil electron: then, the intrinsic spatial resolution in this detector would be limited only by the pad size. Again, as in other semiconductor-based PET scanners described previously, the realization of a stack of such thin detectors (irradiated from the side, Fig. 2.48b, or face-on) would provide axial field coverage with high resolution DOI information [117].

A prototype based on two front Si detector heads (separated by 170 mm) and four BGO detectors (non-position sensitive) has been assembled (Fig. 2.48b shows the Si detector heads), and the performance has been reported for ^{18}F sources [118]. The measured spatial resolution for Si–Si events was 0.98 mm FWHM at the center of the FoV, against a theoretical value (including photon non-collinearity contribution of 0.374 mm FWHM, positron range and source size contributions of 0.254 mm FWHM) of 1.04 mm FWHM. This gave indications that a Si detector with smaller size pads would improve significantly the overall spatial resolution for Si–Si events (e.g., 0.34 mm FWHM for 0.3×0.3 mm^2 pads [115]). Using a ^{18}F line source with 1.1 mm internal diameter, the resolution was 1.45 mm FWHM, with excellent resolution uniformity across the FoV up to 20 mm from the center [117]. Si–Si events contributed only $\cong 1$ % to the system sensitivity, but the consideration of Si–BGO composite events allowed to increase the sensitivity up to 9 %, for a corresponding system resolution of 1 mm FWHM [115].

7   Summary

Most of the commercially available small animal SPECT and PET imaging systems are based on scintillator detectors coupled to position sensitive photomultiplier tubes. The requirement of improved performance, mainly in spatial resolution, has led to the application of microstrip or pixel semiconductor detectors for X-rays and gamma-rays. Compact, high spatial resolution, high energy resolution detector units are now assembled in microSPECT (Table 2.6) and microPET (Table 2.7) scanners.

Table 2.6 Comparison of performance (sensitivity and spatial resolution, simulated or measured for ^{99m}Tc imaging) of semiconductor based small animal SPECT prototypes

System	Technology	Sensitivity (%)	Spatial resolution (mm)	References
Univ. Arizona SPECT/CT	CdZnTe pixel	1×10^{-3}	1–2	[44, 47]
SemiSPECT	CdZnTe pixel	5×10^{-3}	1.45	[48, 59]
SiliSPECT	Si microstrip	7–8×10^{-2}	0.27	[61, 68]
MediSPECT	CdTe pixel	1.6×10^{-2}	<1	[31, 69, 70]
SOLSTICE	CdZnTe strip	NA	<2.5	[11, 53, 81, 82]
LBNL	Si:Li pixel	1.8×10^{-2}	1.6	[30]

For MediSPECT and LBNL, data are reported for ^{125}I imaging (*NA* not available)

Table 2.7 Comparison of performance (sensitivity and spatial resolution, simulated or measured) of semiconductor based small animal PET prototypes (*NA* not available)

System	Technology	Sensitivity (%)	Spatial resolution (mm)	References
SiliPET	Si strips	5.1	0.52	[91–95]
Univ. Tohoku	CdTe strips	1	0.74	[96–100]
Univ. Davis, CA	CdTe strips	3.4	0.5	[101, 102]
Univ. Hokkaido	CdTe	NA	2.6	[103, 104]
SmartPET	HPGe strips	0.99	1.4	[105–112]
CEA-Leti	CdZnTe strips	NA	<1	[89, 113]
CIMA Si-pad	Si pads	1	0.34	[114–118]

This was also possible because of the technical advancements in minute segmentation of the readout electrodes of such detectors, with pitch values well below 1 mm. The potential drawback of the semiconductor detectors—their limited quantum efficiency at medium (140 keV) and high (511 keV) gamma-ray energies, for thin detector substrates—has been bypassed by using side-on irradiation geometries. This allows also to manage the problem of limited active area (a few cm by side) of semiconductor detectors; in fact, for small animal imaging a limited number of closely packed detectors irradiated by their side can be arranged around the animal so as to obtain an adequate FoV coverage. Good spectroscopic performance—often better than scintillator based detectors—is achieved by improved material fabrication and electrical contact technologies, which permit the use of high bias voltages. The major potential for improvement and technological innovation of semiconductor imaging detectors could be in the field of microPET, where high sensitivity ($\approx$4–5 %) with high resolution ($\approx$0.5 mm) are already feasible, as well as integration with semiconductor based microCT. Once available in significant production volumes, all-semiconductor based SPECT/CT and PET/CT systems may contribute to the reduction of the high end-user price of such pre-clinical systems, this being one of the major limitation to the diffusion of small animal imaging systems with ionizing radiation.

References

1. Barrett HH and Hunter WCJ (2005) Detectors for small-animal SPECT I. In: Kupinski MA and Barrett HH (eds.), Small animal SPECT imaging, pp. 26–27. Springer, Heidelberg.
2. (eV Products 2009) http://www.evproducts.com/material_prop.pdf (accessed May 2009).
3. Barrett HH, Eskin JD, and Barber HB (1995) Charge transport in arrays of semiconductor gamma-ray detectors. Phys Rev Lett 5: 156–159.
4. Spartiotis K, Leppänen A, Pantsar T, Pyyhtiä J, Laukka P, Muukkonen K, Maännistö O, Kinnari J, and Schulman T 2005 A photon counting CdTe gamma- and x-ray camera. Nucl Instrum Methods Phys Res A **550**: 267–277.
5. Russo P, Mettivier G, Pani R, Pellegrini R, Cinti MN, and Bennati P (2009) Imaging performance comparison between a LaBr$_3$:Ce scintillator based and a CdTe semiconductor based photon counting compact gamma camera. Med Phys 36: 1298–1317.

6. Guerra P, Santos A, and Darambara DG (2009) An investigation of performance characteristics of a pixellated room-temperature semiconductor detector for medical imaging. J Phys D: Appl Phys 42: 175101.

7. Prokesch M and Szeles C (2006) Accurate measurements of electrical bulk resistivity and surface leakage current of CdZnTe radiation detector crystals. J Appl Phys 100: 014503.

8. Devanathan R, Corrales LR, Gao F, and Weber WJ (2006) Signal variance in gamma-ray detectors—A review. Nucl Instrum Methods Phys Res A **565**: 637–649.

9. "BrilLanCe™380 scintillation material," Technical Data Sheet (2007) (available online at website http://www.detectors.saint-gobain.com/Media/Documents/S0000000000000001004/SGC_BrilLanCe_380_data_sheet.pdf) (accessed May 2009).

10. AMPTEK website (http://www.amptek.com/CdTe.html) (accessed May 2009).

11. Gagnon D, Zeng GL, Links JM, Griesmer JJ, and Valentino FC (2001) Design considerations for a new solid-state gamma-camera: SOLSTICE. Nuclear Science Symposium Conference Record, IEEE, vol. 2: 1156–1160.

12. Ogawa K, Hota A, Shuto K, Motomura N, Kobayashi H, Makino S, Nakahara T, and Kubo A (2006) Development of semiconductor gamma-camera system with CdZnTe detectors. Nuclear Science Symposium Conference Record, 2006, IEEE, vol. 4: 2426–2429.

13. Shulman T (2006) Si, CdTe and CdZnTe radiation detectors for imaging application. PhD thesis, University of Helsinki, Finland, 2006 (available online at website http://ethesis.helsinki.fi/julkaisut/mat/fysik/vk/schulman/sicdtean.pdf) (accessed May 2009).

14. XCOM: Photon Cross Sections Database. Available online at website (http://physics.nist.gov/PhysRefData/Xcom/Text/XCOM.html) (accessed May 2009).

15. ACRORAD Co. website (http://www.acrorad.co.jp/us/cdte.html) (accessed May 2009).

16. Heijne EHM (2001) Semiconductor micropattern pixel detectors: a review of the beginnings. Nucl Instrum Methods Phys Res A **465**: 1–26.

17. Institute of Experimental and Applied Physics, Czech Technical University, Prague, CZ. Available online at website (http://aladdin.utef.cvut.cz/ofat/Methods/Xray_radiography/XrayRadiography.html) (accessed May 2009).

18. Mikulec B, Campbell M, Heijne E, Llopart X, and Tlustos L (2003) X-ray imaging using single photon processing with semiconductor pixel detectors. Nucl Instrum Methods Phys Res A **511**: 282–286.

19. Heijne EHM (2001) Future semiconductor detectors using advanced microelectronics with post-processing, hybridization and packaging technology. Nucl Instrum Methods Phys Res A **541**: 274–285.

20. Alimonti G, Andreazza A, Bulgheroni A, Corda G, Di Gioia S, Fiorello A, Gemme C, Koziel M, Manca F, Meroni C, Nechaeva P, Paoloni A, Rossi L, Rovani A, and Ruscino E (2006) Analysis of the production of ATLAS indium bonded pixel modules. Nucl Instrum Methods Phys Res A **565**: 296–302.

21. Szeles C, Soldner SA, Vydrin S, Graves J, and Bale DS (2008) CdZnTe semiconductor detectors for spectroscopic X-ray imaging. IEEE Trans Nucl Sci **55**: 572–582.

22. Ballabriga R, Campbell M, Heijne EHM, Llopart X, and Tlustos L (2007) The Medipix3 prototype, a pixel readout chip working in single photon counting mode with improved spectrometric performance. IEEE Trans Nucl Sci **54**: 1824–1829.

23. Rönnquist C, Santps F, Toker O, Weilhammer P, Yoshioka K, Nygård E, Czermak E, Jalocha P, Dulinski W, and Hu Y (1994) Double-sided silicon microstrip detectors and low noise self-triggering multichannel readout chips for imaging applications. Nucl Instrum Methods Phys Res A 348: 440–443.

24. Beccherle R Bertolucci E, Bisogni MG, Bottigli U, Collins T, Conti M, Del Guerra A, Fantacci ME, Gambaccini M, Kipnis I, Marchesini R, Marziani M, Rosso V, Russo P, Russo S, Stefanini A, Taibi A, and Tripiccione R (1996) Development of a digital radiography system based on silicon microstrip detector. Physica Medica XII: 17–24.

25. Speller RD, Royle GJ, Triantis FA, Manthos N, Van der Stelt PF, and di Valentin M (2001) Digital X-ray imaging using silicon microstrip detectors: a design study. Nucl Instrum Methods Phys Res A 457: 653–664.

26. Bertolucci E, Conti M, Grossi G, Madonna G, Mancini E, Russo P, Caria M, Randaccio P, Del Guerra A, Gambaccini M, Marchesini R, Marziani M, Taibi A, Beccherle R, Bisogni MG, Bottigli U, Fantacci ME, Rosso V, Stefanini A, Tripiccione R, and Amendolia SR (1996) Autoradiography with silicon strip detectors. Nucl Instrum Methods Phys Res A 381: 527–530.

27. Overdick M, Czermak A, Fischer P, Herzog V, Kjensmo A, Kugelmeier T, Ljunggren K, Nygård E, Pietrzik C, Schwan T, Strand S-E, Straver J, Weilhammer P, Wermes N, and Yoshioka K (1997) A Bioscope system using double-sided silicon microstrip detectors and self-triggering read-out chips. Nucl Instrum Methods Phys Res A 392: 173–177.

28. Chmeissani M and Mikulec B (2001) Performance limits of a single photon counting pixel system. Nucl Instrum Methods Phys Res A 460: 81–90.

29. Beekman FJ, McElroy DP, Berger F, Gambhir SS, Hoffman EJ, and Cherry SR (2002) Towards in vivo nuclear microscopy: iodine-125 imaging in mice using micro-pinholes. Eur J Nucl Med 29: 933–938.

30. Choong WS, Moses WW, Tindall CS, and Luke PN (2005) Design for a high-resolution small-animal SPECT system using pixelated Si:Li detectors for in ^{125}I imaging. IEEE Trans Nucl Sci **52**: 174–180.

31. Accorsi R, Celentano L, Laccetti P, Lanza RC, Marotta M, Mettivier G, Montesi MC, Roberti G, and Russo P (2008) High resolution I-125 small animal imaging with a coded aperture and a hybrid pixel detector. IEEE Trans Nucl Sci **55**: 481–490.

32. Huang AB, Franc BL, Gullberg GT, and Hasegawa BH (2008) Assessment of the sources of error affecting the quantitative accuracy of SPECT imaging in small animals. Phys Med Biol 53: 2233–2252.

33. Belcari N, Bisogni MG, Carpentieri C, Del Guerra A, Delogu P, Panetta D, Quattrocchi M, Rosso V, and Stefanini A (2007) Preliminary characterization of a single photon counting detection system for CT application. Nucl Instrum Methods Phys Res A 576: 204–208.

34. Chmeissani M, Frojdh C, Gal O, Llopart X, Ludwig J, Maiorino M, Manach E, Mettivier G, Montesi MC, Ponchut C, Russo P, Tlustos L, and Zwerger A (2004) First experimental tests with a CdTe photon counting pixel detector hybridized with a Medipix2 readout chip. IEEE Trans Nucl Sci **51**: 2379–2385.

35. Blanchot G, Chmeissani M, Díaz A, Díaz F, Fernández J, García E, García J, Kainberger F, Lozano M, Maiorino M, Martínez R, Montagne JP, Moreno I, Pellegrini G, Puigdengoles C, Sentís M, Teres L, Tortajada M, and Ullán M (2006) Dear-Mama: a photon-counting X-ray imaging project for medical applications. Nucl Instrum Methods Phys Res A 569: 136–139.

36. Autiero M, Celentano L, Cozzolino R, Laccetti P, Marotta M, Mettivier G, Montesi MC, Riccio P, Roberti G, and Russo P (2005) Experimental study on in vivo optical and radionuclide imaging in small animals. IEEE Trans Nucl Sci **52**: 205–209.

37. Funaki M, Ando Y, Jinnai R, Tachibana A, and Ohno R (2007) Development of CdTe detectors in Acrorad. *International Workshop on Semiconductor PET*. Unpublished. Available online at website (http://www.acrorad.co.jp/pdf/Development_of_CdTe_detectors.pdf) (accessed May 2009).

38. Marks DG, Barber HB, Apotovsky BA, Augustine FL, Barrett HH, Dereniak EL, Doty FP, Eskin JD, Hamilton WJ, Matherson KJ, Venzon JE, Woolfenden JM, and Young ET (1996) A 48×48 CZT array with multiplexer readout. IEEE Trans Nucl Sci **43**: 1253–1259.

39. Matherson KJ, Barber HB, Barrett HH, Eskin JD, Dereniak EL, Marks DG, Woolfenden JM, Young ET, and Augustine FL (1998) Progress in the development of large-area modular 64×64 CdZnTe imaging arrays for nuclear medicine. IEEE Trans Nucl Sci **45**: 354–358.

40. Basolo S, Berar JF, Boudet N, Breugnoa P, Chantepia B, Clemens JC, Delpierre P, Dinkespiler B, Hustache S, Medjoubi K, Menouni M, Morel C, Pangaud P, and Vigeolas EA (2008) 20 k pixels CdTe photon-counting imager using XPAD chip. Nucl Instrum Methods Phys Res A 589: 268–274.

41. Takahashi T, Wataname S, Kouda M, Sato G, Okada Y, Kubo S, Kuroda Y, Onishi M, and Ohno R (2001) High-resolution CdTe detector and applications to imaging devices. IEEE Trans Nucl Sci **48**: 287–291.

42. Meng L-J, Tan JW, Spartiotis K, and Schulman T (2009) Preliminary evaluation of a novel energy-resolved photon-counting gamma ray detector. Nucl Instrum Methods Phys Res A **604**: 548–554.
43. Mitani T, Nakamura H, Uno S, Takahashi T, Nakazawa K, Watanabe S, Tajima H, Nomachi M, Fukazawa Y, Kubo S, Kuroda Y, Onishi M, and Ohno R (2003) Large area Gamma-ray Imaging Detector Based on High Resolution CdTe Diode. IEEE Trans Nucl Sci **50**: 1048–1052.
44. Kastis GA, Wu MC, Balzer SJ, Wilson DW, Furenlid LR, Stevenson G, Barrett HH, Barber HB, Woolfenden JM, Kelly P, and Appleby M (2002) Tomographic small-animal imaging using a high-resolution semiconductor detector. IEEE Trans Nucl Sci **49**: 172–175.
45. Chambron J, Arntz Y, Eclancher B, Scheiber Ch, Siffert P, Hage Hali M, Regal R, Kazandjian A, Prat V, Thomas S, Warren S, Matz R, Jahnke A, Karman M, Pszota A, and Nemet L (2000) A pixelated γ-camera based on CdTe detectors clinical interests and performances. Nucl Instrum Methods Phys Res A **448**: 537–549.
46. Tsuchimochi M, Sakahara H, Hayama K, Funaki M, Ohno R, Shirahata T, Orskaug T, Maehlum G, Yoshioka K, and Nygard E (2003) A prototype small CdTe gamma camera for radioguided surgery and other imaging applications. Eur J Nucl Med Mol Imaging **30**: 1605–1614.
47. Kastis GA, Furenlid LR, Wilson DW, Peterson TE, Barber HB, and Barrett HH (2004) Compact CT/SPECT small-animal imaging system. IEEE Trans Nucl Sci **51**: 63–67.
48. Kim H, Furenlid LR, Crawford MJ, Wilson DW, Barber HB, Peterson TE, Hunter WCJ, Liu Z, Woolfenden JM, and Barrett HH (2006) SemiSPECT: A small-animal single-photon emission computed tomography SPECT imager based on eight cadmium zinc telluride (CZT) detector arrays. Med Phys **33**: 465–474.
49. Parnham KB, Grosholz J, Davis RK, Vydrin S, and Cupec CA (2001) Development of a CdZnTe-based small field of view gamma camera. Proc SPIE **4508**: 134–140.
50. Wagenaar DJ, Chowdhury S, Engdahl JC, and Burckhardt DD (2003) Planar image quality comparison between a CdZnTe prototype and a standard NaI(Tl) gamma camera. Nucl Instrum Methods Phys Res A **505**: 586–589.
51. Eisen Y, Mardor I, Shor A, Baum Z, Bar D, Feldman G, Cohen H, Issac E, Haham-Zada R, Blitz S, Cohen Y, Glick B, Falk R, Roudebush S, and Blevis I (2002) NUCAM3—A gamma camera based on segmented monolithic CdZnTe Detectors. IEEE Trans Nucl Sci **49**: 1728–1732.
52. Eisen Y, Shor A, and Mardor I (2004) CdTe and CdZnTe x-ray and gamma-ray detectors for imaging systems. IEEE Trans Nucl Sci **51**: 1191–1198.
53. Griesmer JJ, Kline B, Grosholz J, Parnham K, and Gagnon D (2001) Performance evaluation of a new CZT detector for nuclear medicine: SOLSTICE. Nuclear Science Symposium Conference Record, IEEE, vol. 2: 1050–1054.
54. Azman S, Gjaerum J, Meier D, Muftuler LT, Maehlum G, Nalcioglu O, Patt BE, Sundal B, Szawlowski M, Tsui BMW, Wagenaar DJ, and Wang Y (2007) A nuclear radiation detector system with integrated readout for SPECT/MR small animal imaging. Nuclear Science Symposium Conference Record, IEEE, vol. 3: 2311–2317.
55. Mestais C, Baffert N, Bonnefoy JP, Chapuis A, Koenig A, Monnet O, Ouvrier Buffet P, Rostaing JP, Sauvage F, and Verger L (2001) A new design for a high resolution, high efficiency CZT gamma camera detector. Nucl Instrum Methods Phys Res A **458**: 62–67.
56. Barber HB, Barrett HH, Augustine F., Hamilton WJ, Apotovsky BA, Dereniak EL, Doty FP, Eskin JD, Garcia JP, Marks DG, Matherson KJ, Woolfenden JM, and Young ET (1997) Development of a 64×64 CZT array and associated readout integrated circuit for use in nuclear medicine. J Electron Mater **26**: 765–772.
57. Kastis GA, Barber HB, Barrett HH, Balzer SJ, Lu D, Marks DG, Stevenson G, Woolfenden JM, Appleby M, and Tueller J (2000) Gamma-ray imaging using a CdZnTe pixel array and a high-resolution, parallel-hole collimator. IEEE Trans Nucl Sci 47: 1923–1927.
58. http://www.radiology.arizona.edu/CGRI/research-projects/animal.html (accessed May 2009).

59. Peterson TE, Hyunki K, Crawford MJ, Gersham BM, Hunter WCJ, Barber HB, Furenlid LR, Wilson DW, Woolfenden JM, and Barrett HH (2002) SemiSPECT: a small-animal imaging system based on eight CdZnTe pixel detector. Nuclear Science Symposium Conference Record (2002), IEEE, vol. 3: 1844–1847.

60. http://www.radiology.arizona.edu/CGRI/research-projects/Adaptive_Modality_Imaging/adaptive_modality.html (accessed May 2009).

61. Shokouhi S, Fritz MA, McDonald BS, Wilson M.D., Metzler SD, and Peterson TE (2006) Design of a Multi-Pinhole Collimator in a Dual-Headed, Stationary, Small-Animal SPECT. Nuclear Science Symposium Conference Record, IEEE, vol. 4: 2399–2402.

62. Shokouhi S, Durko HL, Fritz MA, Furenlid LR, and Peterson TE (2006) Thick silicon strip detectors for small-animal SPECT imaging. Nuclear Science Symposium Conference Record, IEEE, vol. 6: 3562–3566.

63. McDonald BS, Shokouhi S, Barrett HH, and Peterson TE (2006) Multi-energy, single-isotope pinhole imaging using stacked detectors. Nuclear Science Symposium Conference Record (2006), IEEE, vol. 3: 1797–1801.

64. Shokouhi S, McDonald BS, Durko HL, Fritz MA, Furenlid LR, Peterson TE (2007) Performance characteristics of thick silicon double sided strip detectors. Nuclear Science Symposium Conference Record, IEEE, vol. 2: 1656–1660.

65. Shokouhi S, Fritz MA, McDonald BS, Durko HL, Furenlid LR, Wilson DW, and Peterson TE (2007) A silicon SPECT system for molecular imaging of the mouse brain. Nuclear Science Symposium Conference Record, IEEE, vol. 4: 2782–2784.

66. Shokouhi S, Wilson DW, Pham W, and Peterson TE (2007) System evaluation for in vivo imaging of amyloid beta plaques in a mouse brain using statistical decision theory. Nuclear Science Symposium Conference Record, IEEE, vol. 6: 4528–4530.

67. http://www.radiology.arizona.edu/CGRI/SiliSPECT.pdf (accessed May 2009).

68. Shokouhi S, Metzler SD, Wilson DW, and Peterson TE (2009) Multi-pinhole collimator design for small-object imaging with SiliSPECT: a high resolution SPECT. Phys Med Biol 54: 207–225.

69. Accorsi R, Autiero M, Celentano L, Chmeissani M, Cozzolino R, Curion AS, Frallicciardi P, Laccetti P, Lanza RC, Lauria A, Maiorino M, Marotta M, Mettivier G, Montesi MC, Riccio P, Roberti G, and Russo P (2007) MediSPECT: Single photon emission computed tomography system for small field of view small animal imaging based on a CdTe hybrid pixel detector. Nucl Instrum Methods Phys Res A **571**: 44–47.

70. Accorsi R, Curion AS, Frallicciardi P, Lanza RC, Lauria A, Mettivier G, Montesi MC, and Russo P (2007) Preliminary evaluation of the tomographic performance of the MediSPECT small animal imaging system. Nucl Instrum Methods Phys Res A **571**: 415–418.

71. Autiero M, Celentano L, Cozzolino R, Laccetti P, Marotta M, Mettivier G, Montesi MC, Riccio P, Roberti G, and Russo P (2006) Multimodal system for in vivo tumor imaging in mice. Proc SPIE 6191: 340–352.

72. Llopart X, Campbell M, Dinapoli R, SanSegundo D, and Pernigotti E (2002) Medipix2, a 64 k pixel read-out with 55 μm square elements working in single photon counting mode. IEEE Trans Nucl Sci **49**: 2279–2283.

73. Medipix2 collaboration website: www.cern.ch/medipix (accessed May 2009).

74. Russo P (2002) Hybrid semiconductor pixel detectors for low- and medium-energy X- and gamma-ray single photon imaging using the Medipix read-out chip. In: Hornak JP (ed.), *Encyclopedia of Imaging Science and Technology*. Wiley Interscience, John Wiley & Sons, Inc., New York.

75. Tlustos L, Ballabriga R, Campbell M, Heijne E, Kincade K, Llopart X, and Stejskal P (2006) Imaging properties of the Medipix2 system exploiting single and dual energy thresholds. IEEE Trans Nucl Sci **53**: 367–372.

76. Mettivier G, Montesi MC, Sebastiano A, and Russo P (2006) High frame rate X-ray imaging with a 256×256 pixel single photon counting Medipix2 detector. IEEE Trans Nucl Sci **53**: 1650–1655.

77. Maiorino M, Pellegrini G, Blanchot G, Chmeissani M, Garcia J, Martinez R, Lozano M, Puigdengoles C, and Ullan M (2006) Charge sharing observations with a CdTe pixel detector irradiated with a ^{57}Co source. Nucl Instrum Methods Phys Res A **563**: 177–181.

78. Pellegrini G, Chmeissani M, Maiorino M, Blanchot G, Garcia J, Lozano M, Martinez R, Puigdengoles C, Ullan M, and Casado P (2006) Performance limits of a 55-μm pixel CdTe detector. IEEE Trans Nucl Sci **53**: 361–366.

79. Pellegrini G, Maiorino M, Blanchot G, Chmeissani M, Garcia J, Lozano M, Martinez R, Puigdengoles C, and Ullan M (2007) Direct charge sharing observation in single-photon-counting pixel detector. Nucl Instrum Methods Phys Res A **573**: 137–140.

80. Zeng GL and Gagnon D (2004) CdZnTe strip detector SPECT imaging with a slit collimator. Phys Med Biol 49: 2257–2271.

81. Gagnon D, Penn MS, Lee D, Urbain J-L, Chi-Hua T, Kline B, Bender PJ, Mercer DL, and Griesmer JJ (2002) Use of SOLSTICE rotating slat solid-state camera for small animal imaging. Nuclear Science Symposium Conference Record, IEEE, vol. 3: 1367–1369.

82. Moses WW Nuclear medical imaging: Techniques and challenges. Available online at website (http://instrumentationcolloquium.lbl.gov/Nuclear%20Medical%20Imaging.pdf) (accessed May 2009).

83. Stickel JR and Cherry SR (2005) High-resolution PET detector design: modeling components of intrinsic spatial resolution. Phys Med Biol 50: 179–195.

84. Levin CS and Hoffman EJ (1999) Calculation of positron range and its effects on the fundamental limit of positron emission tomography system spatial resolution. Phys Med Biol 44: 781–799.

85. Drezet A, Monnet O, Montémont G, Rustique J, Sanchez G, and Verger L (2004) CdZnTe detectors for the positron emission tomographic imaging of small animals. Nuclear Science Symposium Conference Record, IEEE, vol. 7: 4564–4568.

86. Conti M, Del Guerra A, Mazzei D, Russo P, Bencivelli W, Bertolucci E, Messineo A, Rosso V, Stefanini A, Bottigli U, Randaccio P, and Nelson WR (1992) Use of EGS4 Monte Carlo code to evaluate the response of HgI2 and CdTe semiconductor detectors in the diagnostic energy range. Nucl Instrum Methods Phys Res A 322: 591–595.

87. Baldazzi G, Bollini D, Casali F, Chirco P, Donati A, Dusi W, Landini G, Rossi M, and Stephen JB (1993) Timing response of CdTe detectors. Nucl Instrum Methods Phys Res A 326: 319–324.

88. Bertolucci E, Conti M, Curto CA, and Russo P (1997) Timing properties of CdZnTe detectors for positron emission tomography. Nucl Instrum Methods Phys Res A **400**: 107–112.

89. Drezet A, Monnet O, Mathy F, Montémont G, and Verger L (2007) CdZnTe detectors for small field of view positron emission tomographic imaging. Nucl Instrum Methods Phys Res A **571**: 465–470.

90. Vaska P, Bolotnikov A, Carini G, Camarda G, Pratte J-F, Dilmanian FA, Park S-J, and James RB (2005) Studies of CZT for PET Applications. Nuclear Science Symposium Conference Record, IEEE, vol. 5: 2799–2802.

91. Zavattini G, Cesca N, Di Domenico G, Moretti E, and Sabba N (2006) SiliPET: an ultra high resolution design of a small animal PET scanner based on double sided silicon strip detector stacks. Nucl Instrum Methods Phys Res A **568**: 393–397.

92. Auricchio N, Cesca N, Di Domenico G, Moretti E, Sabba N, Gambaccini M, Zavattini G, Andritschke R, Kanbach G, and Schopper F (2005) SiliPET: design of an ultra high resolution small animal PET scanner based on stacks of semiconductor detectors. Nuclear Science Symposium Conference Record, IEEE, vol. 5: 3010–3013.

93. Gola A, Fiorini C, Di Domenico G, Zavattini G, and Auricchio N (2006) An ASIC circuit for timing measurements with strip detectors, designed for the SiliPET project. Nuclear Science Symposium Conference Record, IEEE, vol. 1: 370–374.

94. Auricchio N, Di Domenico G, Zavattini G, Gola A, Fiorini C, Frigerio M, Ambrosi G, Ionica M, Fiandrini E, Zorzi N, and Boscardin M (2007) First measurements of the SiliPET project: a small animal PET scanner based on stacks of silicon detectors. Nuclear Science Symposium Conference Record, IEEE, vol. 4: 2926–2929.

95. Auricchio N.; Di Domenico G.; Milano L.; Malaguti R.; Ambrosi G, Ionica M, Fiandrini E, Zorzi N, Boscardin M, and Zavattini G (2008) Experimental measurements for the SiliPET project: a small animal PET scanner based on stacks of silicon detectors. Nuclear Science Symposium Conference Record, IEEE: 366–369.

96. Kikuchi Y, Ishii K, Yamazaki H, Matsuyama S, Yamaguchi T, Yamamoto Y, Sato T, Aoki Y, and Aoki K (2005) Preliminary report on the development of a high resolution PET camera using semiconductor detectors. Nucl Instrum Methods Phys Res B **241**: 727–731.

97. Kikuchi Y, Ishii K, Yamazaki H, Matsuyama S, Momose G, Ishizaki A, Kisaka J, and Kudo T (2006) Feasibility of ultra high resolution better than 1 mm FWHM of small animal PET by using CdTe detector arrays. Nuclear Science Symposium Conference Record, IEEE, vol. 4: 2454–2457.

98. Ishii K, Kikuchi Y, Matsuyama S, Kanai Y, Kotani K, Ito T, Yamazaki H, Funaki Y, Iwata R, Itoh M, Kanai Km Hatazawa J, Itoh N, Tanizaki N, Amano D, Yamada M, and Yamaguchi T (2007) First achievement of less than 1 mm FWHM resolution in practical semiconductor animal PET scanner. Nucl Instrum Methods Phys Res A **576**: 435–440.

99. Kikuchi Y, Ishii K, Terakawa A, Matsuyama S, Yamazaki H, Hatazawa J, and Kotani K (2007) Prototype of high resolution PET using resistive electrode position sensitive CdTe detectors. Nuclear Science Symposium Conference Record, IEEE, vol. 4: 2669–2672.

100. Kikuchi Y, Ishii K, Yamazaki H, Matsuyama S, Nakhostin M, Sakai T, Nakamura K, and Kouno M (2008) Fundamental study of two-dimensional position sensitive CdTe detector for PET camera. Nuclear Science Symposium Conference Record, IEEE, vol. 4: 4924–4926.

101. Kim H, Cirignano LJ, Dokhale P, Bennet P, Stickel JR, Mitchell GS, Cherry SR, Squillante M, and Shah K (2006) CdTe orthogonal strip detector for small animal PET. Nuclear Science Symposium Conference Record, IEEE, vol. 6: 3827–3830.

102. Mitchell GS, Sinha S, Stickel JR, Bowen SL, Cirignano LJ, Dokhale P, Kim H, Shah K, and Cherry SR (2008) CdTe strip detector characterization for high resolution small animal PET. IEEE Trans Nucl Sci **55**: 870–876.

103. Yanagita N, Morimoto Y, Ishitsu T, Suzuki A, Takeuchi W, Seino T, Takahashi I, Ueno Y, Amemya K, Inoue S, Suzuki M, Kozawa F, Kubo N, and Tamaki N (2007) Physical performance of a prototype 3D PET scanner using CdTe detectors. Nuclear Science Symposium Conference Record, IEEE, vol. 4: 2665–2668.

104. Ueno Y, Morimoto Y, Tsuchiya K, Yanagita N, Kojima S, Ishitsu T, Kitaguchi H, Kubo N, Zhao S, Tamaki N, and Amemiya K (2009) Basic performance test of a prototype PET scanner using CdTe semiconductor detectors. IEEE Trans Nucl Sci **56**: 24–28.

105. Hall CJ, Nolan PJ, Boston AJ, Helsby WI, Berry A, Lewis RA, Gillam J, Beveridge T, Mather AR, Turk G, Norman J, and Gross S (2003) A gamma tracking detector for nuclear medicine. Nuclear Science Symposium Conference Record, IEEE, vol. 3: 1877–1881.

106. Boston HC, Boston AJ, Cooper RJ, Cresswell J, Grint AN, Mather AR, Nolan PJ, Scraggs DP, Turk G, Hall CJ, Lazarus I, Berry A, Beveridge T, Gillam J, and Lewis R (2007) Characterization of the SmartPET planar Germanium detectors. Nucl Instrum Methods Phys Res A **579**: 104–107.

107. Gillam J, Beveridge T, Svalbe I, Grint A, Cooper R, Boston A, Boston H, Nolan P, Hall C, and Lewis R (2008) Compton imaging using the SmartPET detectors. Nuclear Science Symposium Conference Record, IEEE: 624–628.

108. http://ns.ph.liv.ac.uk/imaging-group/group-members/andrew-mather.php (accessed August 2009).

109. Cooper RJ, Boston AJ, Boston HC, Cresswell J, Grint AN, Mather AR, Nolan PJ, Scraggs DP, Turk G, Hall CJ, Lazarus I, Berry A, Beveridge T, Gillam J, and Lewis RA (2007) SmartPET: applying HPGe and pulse shape analysis to small-animal PET. Nucl Instrum Methods Phys Res A **579**: 313–317.

110. Cooper RJ, Turk G, Boston AJ, Boston HC, Cresswell J, Mather AR, Nolan PJ, Hall CJ, Lazarus I, Simpson J, Berry A, Beveridge T, Gillam J, and Lewis RA (2007) Position sensitivity of the first SmartPET HPGe detector. Nucl Instrum Methods Phys Res A **573**: 72–75.

111. Cooper RJ, Boston AJ, Boston HC, Cresswell JR, Grint AN, Harkness LJ, Nolan PJ, Oxley DC, D.P. Scraggs DP, Lazarus I, Simpson J, Dobson J (2008) Charge collection performance of a segmented planar high-purity germanium detector. Nucl Instrum Methods Phys Res A **595**:401–409.
112. Cooper RJ, Boston AJ, Boston HC, Cresswell J, Grint AN, Harkness LJ, Nolan PJ, Oxley DC, Scraggs DP, Mather AR, Lazarus I, and Simpson J (2009) Positron emission tomography imaging with the SmartPET system. Nucl Instrum Methods Phys Res A **606**: 523–532.
113. Peyret O (2006) Towards digital X-ray imaging. Available online at website(http://www.minatec-crossroads.com/pdf-AR/Peyret.pdf) (accessed August 2009).
114. CIMA Collaboration website (http://www.cima-collaboration.org).
115. Park S-J, Rogers WL and Clinthorne NH (2007) Design of a very high-resolution small animal PET scanner using a silicon scatter detector. Phys Med Biol 52: 4653–4677.
116. Clinthorne N (2009) Methods for High Resolution PET. Stanford Linear Accelerator Center, Advanced Instrumentation Seminar, 1April 2009. Available online at website (http://www-group.slac.stanford.edu/ais/publicDocs/presentation113.pdf) (accessed August 2009).
117. Park S-J, Rogers WL, Huh S, Kagan H, Honscheid K, Burdette D, Chesi E, Lacasta C, Llosa G, Mikuz M, Studen A, Weilhammer P, and Clinthorne NH (2007) A prototype of very high-resolution small animal PET scanner using silicon pad detectors. Nucl Instrum Methods Phys Res A **570**: 543–555.
118. Park S-J, Rogers WL, Huh S, Kagan H, Honscheid K, Burdette D, Chesi E, Lacasta C, Llosa G, Mikuz M, Studen A, Weilhammer P, and Clinthorne NH (2007) Performance evaluation of a very high resolution small animal PET imager using silicon scatter detectors. Phys Med Biol 52: 2807–2826.